A silent Kv channel subunit shapes PV neuron action potential waveform and short-term synaptic plasticity during high-frequency firing

Sanika Ganesh[1], Theresa M. Canty[1], Bernardo L. Sabatini[1*]

[1] Howard Hughes Medical Institute, Department of Neurobiology, Harvard Medical School, Boston, MA 02115, USA.

* Bernardo L. Sabatini
Email: bsabatini@hms.harvard.edu

Author Contributions: S.G. and B.L.S. designed research; S.G. and T.C. performed research; S.G., T.C., and B.L.S. analyzed data; S.G. and B.L.S. wrote the paper.

Competing Interest Statement: The authors declare no competing interests.

Classification: Biological Sciences, Neuroscience

Keywords: PV neuron, potassium channel, silent subunit, GABAergic, inhibition

This PDF file includes:

Main Text
Figures 1 to 5

Abstract

Fast-spiking parvalbumin-positive (PV) neurons provide precisely timed, context-dependent inhibition within cortical circuits. PV neuron firing properties are specialized among cortical neurons, suggesting that they express a unique complement of ion channels. Here, we identify the PV-specific silent voltage-gated potassium (Kv) channel subunit Kv6.4 (encoded by *Kcng4*) as a modulator of both intrinsic and synaptic properties. Kv6.4 does not form functional channels on its own but assembles with Kv2 subunits to create heterotetrameric channel complexes. *Kcng4* expression is enriched within a distinct *Pvalb*-expressing subclass in primary somatosensory (S1) and motor (M1) cortex and emerges during postnatal development. Kv6.4 depolarizes the interspike and threshold potentials, broadens action potentials (APs), increases AP height, and decelerates the AP upstroke. These changes in AP waveform enhance GABA release probability and paired-pulse depression at synapses made by PV onto pyramidal (PYR) neurons. The effects of Kv6.4 loss are amplified during high-frequency firing, within the physiological range of fast-spiking PV neurons, likely due to altered repolarization dynamics that accumulate across successive APs. These findings are thus consistent with the function of Kv6.4 in modifying Kv2-mediated delayed rectifier currents. Hence, Kv6.4 tunes the temporal precision of PV inhibitory output, a feature that may be critical for stable excitation-inhibition ratios and adaptive circuit function underlying learning and behavior.

Significance Statement

Voltage-gated ion channels are broadly expressed yet serve cell-type-specific functions. We demonstrate that the Kv6.4 silent subunit is selectively expressed by fast-spiking parvalbumin-positive (PV) inhibitory neurons among cortical neurons. In PV neurons, Kv6.4 modulates action potential (AP) waveform and GABA release probability onto excitatory neurons in a frequency-dependent manner, well within the physiological range of PV firing. This mechanism is likely important for preserving the temporal precision of inhibition, which is particularly critical for fast-

spiking interneuron output. By shaping short-term synaptic plasticity during high-frequency firing, Kv6.4 provides a molecular and cell-type-specific mechanism for context-dependent tuning of inhibition within cortical circuits. This function may be especially relevant for sensory processing, experience-dependent plasticity, and the maintenance of excitation-inhibition ratios *in vivo*.

Main Text

Introduction

The specific combination of ion channels expressed by each neuron shapes its physiological properties. Large-scale transcriptional analyses have systematically mapped and characterized the molecular signatures of many neuronal classes (1–10), yielding new insights into the variability of ion channel composition across cell classes. These transcriptional data can be integrated with electrophysiological analyses to reveal the mechanisms that govern the intrinsic excitability and synaptic properties of distinct neuron types.

In many brain areas, fast-spiking (FS) interneurons have unique electrophysiological characteristics such as the ability to maintain high rates of action potential (AP) firing. In cerebral cortex, fast-spiking parvalbumin-positive (PV) interneurons deliver precisely timed, potent inhibition by targeting the somatodendritic domain of excitatory PYR neurons (11). As the largest class of cortical GABAergic neurons, PV neurons preserve network stability by providing cortical gain control (12–14), regulate the temporal precision of PYR neuron firing (15, 16), and gate experience-dependent plasticity (17, 18), especially during critical periods of cortical development (19). Disruptions in PV-cell-mediated inhibition have been implicated in neurological disorders such as epilepsy, schizophrenia, depression, autism spectrum disorder, and Alzheimer's disease (11, 20).

The diverse functions of PV neurons depend on their capacity for rapid, non-adapting AP firing. Particularly important to sustaining high AP firing rates are potassium (Kv) channels: Kv3 channels support the FS phenotype by facilitating rapid AP repolarization (21–23), whereas Kv1 channels regulate near-threshold excitability by setting AP threshold and first spike latency (24–26). In contrast, the significance of modulatory potassium channel subunits—nonconducting on their own, but capable of powerfully shaping the behavior of channel complexes—remains largely unexplored (27). These "silent" subunits represent a potentially critical yet understudied mechanism for tuning neuronal excitability and circuit dynamics. Notably, their expression is more restricted than that of electrically active channels (28), raising the possibility that their cell-type-specific expression patterns may underlie functional diversity of neuronal classes.

Multiple single-cell transcriptomic datasets indicate that across cerebral cortical neurons, *Kcng4*, a gene that encodes the nonconducting subunit Kv6.4, is selectively expressed in PV interneurons (3, 10). Prior analyses of cultured and peripheral neurons have demonstrated that Kv6.4 co-assembles with Kv2.1 to generate functional Kv2.1/Kv6.4 channels (29–36). Due to alterations of the voltage-sensing domain, these heterotetrameric channels exhibit a ~30-40 mV hyperpolarized shift in their voltage dependence of inactivation compared to Kv2.1 homomers (29, 30, 32–35). How Kv2.1/Kv6.4 channels influence PV neuron physiology has been unknown.

Here, we examine the expression of the Kv6.4 channel subunit in cortical neurons and its contribution to the physiology of PV interneurons. We show that *Kcng4* expression is enriched within *Pvalb*-expressing neurons in primary somatosensory (S1) and motor (M1) cortex. The timing of *Kcng4* expression during postnatal development, together with its spatial distribution, suggest a role in the physiology of mature FS neurons. To examine the function of Kv6.4, we used the Kcng4^{Cre} knock-in mouse line in which Cre recombinase replaces endogenous *Kcng4*, effectively knocking-out the gene. Whole-cell recordings show that Kv6.4 expression modifies AP shape and interspike potentials during repetitive firing without altering AP frequency. At the

synaptic level, paired recordings show that lack of Kv6.4 expression regulates PV inhibition onto nearby PYR neurons during fast spiking, thereby affecting short-term plasticity during rapid firing.

Results

Cortical PV neurons selectively express *Kcng4*

The potassium channel Kv6.4 subunit, encoded by *Kcng4*, forms heterotetrameric channels with Kv2.1, encoded by *Kcnb1*. To characterize the expression of these potassium channel subunits in cortical PV neurons, we performed multiplexed fluorescent *in situ* hybridization (FISH) to examine the expression of *Kcng4*, *Kcnb1*, and *Pvalb* (n=6/18/36 mice/sections/hemispheres per region, 2-4 sections per mouse) in M1 and S1 in wildtype C57BL/6J mice (**Fig. 1 *A-B***).

We detected expression of *Kcng4* across cortical layers in M1 and S1, roughly mirroring that of *Pvalb* (**Fig. 1 *C-D***). High-resolution images demonstrate *Kcng4* and *Pvalb* co-expression within individual cells (**Fig. 1*C***). Indeed, nearly all *Kcng4*+ cells express *Pvalb* (M1: 0.88 ± 0.025, S1: 0.95 ± 0.009), and a substantial proportion of *Pvalb*+ neurons express *Kcng4* (M1: 0.25 ± 0.014, S1: 0.39 ± 0.020), with higher co-expression of *Pvalb* and *Kcng4* in S1 compared to M1 (**Fig. 1*E*** and **Dataset S1**). These cortical co-expression patterns are reminiscent of those observed in PV neurons of the external globus pallidus (GPe), where ~90% of *Kcng4*+ neurons express *Pvalb*, and ~30% of *Pvalb*+ neurons express *Kcng4* (37). In both M1 and S1, co-expression patterns were consistent across layers (L; **Fig. 1*D***). However, we noted high enrichment of *Kcng4* in S1 L4 *Pvalb*+ neurons (S1 L4: 0.70 ± 0.027; **Fig. 1*E*** and **Dataset S1**). We found that almost every neuron that co-expressed *Kcng4* and *Pvalb* also expressed *Kcnb1* (*Kcnb1*: 0.99 ± 0.003; **Dataset S*1***). While most functional studies of Kv6.4 have reported its assembly with Kv2.1 (29–35, 38), Kv2.1 and Kv2.2 (encoded by *Kcnb2*) independently interact with Kv6.4 (36). Both *Kcnb1* and *Kcnb2* are expressed by PV neurons (**Fig. S1*C***).

The results of these FISH analyses are consistent with spatial transcriptomic data from the Allen Brain Cell Atlas (10), which confirm that *Kcng4* is selectively expressed in *Pvalb*+ neurons in M1 and S1 (**Fig. S1*A***). We also noted that *Kcng4*+ neurons comprise a unique transcriptionally defined supertype (supertype 207) of *Pvalb*+ interneurons (**Fig. S1*B***), as previously defined (10).

Spatiotemporal patterns of Kcng4^{Cre} activation

Pvalb expression emerges around postnatal day (P) 12, and PV neuron maturation restricts critical periods of heightened sensory-motor cortical plasticity (18, 19, 25, 39). Therefore, we examined the onset of Kv6.4 expression. We generated Kcng4^{Cre}; Ai14 mice by crossing a transgenic mouse line in which Cre is knocked into the *Kcng4* locus (Kcng4^{Cre}), resulting in a functional knock-out, to a reporter line that expresses tdTomato in a Cre-dependent manner (Ai14). We used tdTomato fluorescence to compare Kcng4^{Cre} activation in M1 and S1 of young (2 weeks) and adult (5+ weeks) heterozygous (Kcng4$^{Cre/WT}$; Ai14) and homozygous (Kcng4$^{Cre/Cre}$; Ai14) mice (**Fig. 2*A***). We detected weak tdTomato fluorescence in young mice and strong fluorescence in M1 and S1 of adult mice (**Fig. 2 *B-D***). High-resolution imaging at the 2-week timepoint revealed that tdTomato-labeled cortical cells in young animals exhibit astrocytic morphology, characterized by extensive arborization and a lack of polarized processes (**Fig. S2 *A-C***). These results suggest that there is minimal Kcng4^{Cre} activation, if any, in PV neurons at early developmental stages, and that Kv6.4 expression arises after maturation of PV neurons.

In adult mice, Kcng4^{Cre}-mediated expression of tdTomato occurs in brain regions that contain fast-spiking neurons, such as the cerebral cortex, GPe, and cerebellum (**Fig. S*3***). *Kcng4*+ neurons have previously been identified as a subclass of PV neurons in the GPe, and in the cerebellum, *Kcng4* expression is enriched in fast-spiking Purkinje cells (**Fig. S1*D)***, which include PV neurons (6, 37). The spatial distribution of tdTomato+ neurons is consistent with Kv6.4

155 expression in fast-spiking neuronal populations across multiple brain regions. Together, the
156 spatial and temporal patterns of Kcng4^{Cre} activation raise the possibility that Kv6.4 shapes the
157 fast-spiking phenotype of PV neurons.
158
159 **Kv6.4 modulates AP height, AP half-width, and interspike potential in PV neurons**
160
161 To study the role of Kv6.4 in PV neuron physiology, we performed whole-cell current-clamp
162 recordings in fast-spiking neurons from L2/3 wildtype *Kcng4* (n=18/4 cells/mice; PV$^{Cre/WT}$; Ai14),
163 heterozygous *Kcng4* knock-out (n=16/4; Kcng4$^{Cre/WT}$; Ai14), and homozygous *Kcng4* knock-out
164 (n=20/4; Kcng4$^{Cre/Cre}$; Ai14) mice carrying two (WT/WT), one (Cre/WT), or no (Cre/Cre) copies of
165 *Kcng4*, respectively. In each genotype, recordings were made from tdTomato-expressing neurons
166 in age-matched adult animals. Because S1 *Pvalb*+ neurons are more likely to express *Kcng4*
167 than M1 *Pvalb*+ neurons (**Fig. 1*E***), we conducted electrophysiological recordings in S1. We used
168 a series of current injections to measure voltage (-200 to 200 pA, 40 pA increments) and AP (200
169 to 1200 pA, 100 pA increments) responses across all three genotypes, blinded to heterozygous
170 and homozygous animals from which acute brain slices were prepared (**Fig. 3*A***). We used
171 littermates to compare heterozygous and homozygous animals. We observed no significant
172 differences in current–voltage or current–firing rate relationships across genotypes (**Fig. 3*B*** and
173 **Dataset S2**).
174
175 However, AP height, AP half-width, and interspike potential differed significantly between groups
176 (**Fig. 3 *C-F*** and **Dataset S2*)***. To standardize analysis across cells with varying rheobase, we
177 analyzed the first trace containing at least 10 APs and restricted analysis to the 2nd and 10th APs
178 in these traces to survey early and later phases of the AP train. AP height was lower in
179 homozygous mice compared to wildtype for the 2nd AP (WT/WT = 85.05 ± 1.00 mV, Cre/WT =
180 82.84 ± 1.10 mV, Cre/Cre = 81.44 ± 0.95 mV; one-way ANOVA, p = 0.041; Tukey–Kramer post
181 hoc comparisons: WT/WT vs Cre/WT p = 0.297, WT/WT vs Cre/Cre p = 0.032, Cre/WT vs
182 Cre/Cre p = 0.597), and for the 10th AP (**Fig. 3 *C-D*** and **Dataset S2**). Half-width was also
183 significantly reduced in homozygous mice, both for the 2nd AP (WT/WT = 0.22 ± 0.01 ms, Cre/WT
184 = 0.23 ± 0.01 ms, Cre/Cre = 0.20 ± 0.01 ms; one-way ANOVA, p = 0.007; Tukey–Kramer post
185 hoc comparisons: WT/WT vs Cre/WT p = 0.911, WT/WT vs Cre/Cre p = 0.030, Cre/WT vs
186 Cre/Cre p = 0.013) and the 10th AP (**Fig. 3 *E-F*** and **Dataset S2**). Additionally, the interspike
187 potential, defined as the most negative potential between APs, was more negative in
188 homozygous mice for the 2nd AP (WT/WT = -69.55 ± 0.86 mV, Cre/WT = -68.81 ± 0.83 mV,
189 Cre/Cre = -71.87 ± 0.72 mV; one-way ANOVA, p = 0.022; Tukey–Kramer post hoc comparisons:
190 WT/WT vs Cre/WT p = 0.805, WT/WT vs Cre/Cre p = 0.098, Cre/WT vs Cre/Cre p = 0.026) and
191 the 10th AP (**Fig. 3 *G-H*** and **Dataset S2**). Bootstrapping analysis further confirmed differences in
192 the distributions across groups (**Fig. 3 *C, E,* and *G***). These results indicate that Kv6.4 loss
193 decreases AP amplitude and duration and deepens the interspike potential in PV neurons. These
194 effects are consistent with Kv6.4 normally reducing Kv2 current by causing heterotetramers to
195 inactivate at more negative potentials.
196
197 We also examined additional intrinsic properties of fast-spiking neurons across the three groups,
198 such as the AP threshold, AP maximum slope, afterhyperpolarization (AHP) amplitude for a train
199 of APs, and sag voltage. We found that the three groups differed significantly in AP threshold for
200 the 10th AP (WT/WT = -42.14 ± 0.81 mV, Cre/WT = -42.00 ± 0.58 mV, Cre/Cre = -44.14 ± 0.60
201 mV; one-way ANOVA, p = 0.046; Tukey–Kramer post hoc comparisons: WT/WT vs Cre/WT p =
202 0.988, WT/WT vs Cre/Cre p = 0.090, Cre/WT vs Cre/Cre p = 0.076), but not for the 2nd AP (**Fig.
203 S4 *A-B*** and **Dataset S2**), suggesting that Kv6.4 contributes to maintaining a more depolarized
204 AP threshold particularly over the course of repetitive firing (**Fig. S4*B***). AP maximum slope was
205 also significantly higher at the 10th AP in homozygous mice (WT/WT = 452.02 ± 11.98 V/s,
206 Cre/WT = 432.02 ± 22.33 V/s, Cre/Cre = 488.23 ± 13.40 V/s; one-way ANOVA, p = 0.047;
207 Tukey–Kramer post hoc comparisons: WT/WT vs Cre/WT p = 0.666, WT/WT vs Cre/Cre p =
208 0.233, Cre/WT vs Cre/Cre p = 0.042), but no differences were observed at the 2nd AP (**Fig. S4 *C-***

209 ***D*** and **Dataset S2**). Thus, when Kv6.4 is absent, fast-spiking neurons appear to exhibit an
210 increased upstroke velocity during repetitive firing. There were no significant differences in the
211 AHP amplitude (**Fig. S4 *E-F*** and **Dataset S2**) or sag voltage (**Fig. S4 *G-H*** and **Dataset S2**).
212 These results indicate that Kv6.4 contributes to maintaining a more depolarized AP threshold and
213 limiting the AP upstroke velocity during sustained firing in PV neurons.
214
215 Additionally, we analyzed AP height, half-width, interspike potential, threshold potential, and
216 maximum slope across all recordings, with data organized into bins containing comparable
217 numbers of APs (**Fig. S5*A***), and found that differences in genotype persist across firing rates
218 (**Fig. S5 *B-F***). Thus, group differences in these metrics are robust to the trace selection criterion
219 described previously (2nd and 10th AP within the first trace containing ≥10 APs for the analysis
220 shown in ***Fig. 2*** and ***Fig. S4***). The shorter AP duration in homozygous animals is not attributable
221 to adaptation of the interspike interval (ISI; ms), as the groups exhibit a similar change (Δ) in ISI
222 between early and late spikes ($ISI_{49-50} – ISI_{2-3}$) in recordings containing ≥50 APs (**Fig. S5*G***).
223 Homozygous animals, however, display within-trace adaptation in AP half-width and interspike
224 potential between early and late spikes ($AP_{50} – AP_2$; **Fig. S5 *H-I***). Furthermore, adaptation in AP
225 half-width becomes more pronounced at higher firing rates (**Fig. S5*H***). Hence, Kv6.4 loss
226 deepens the interspike potential and shortens action potentials, with increasing effects at higher
227 firing frequencies.
228
229 Especially during repetitive firing, Kv6.4 deletion yields more negative interspike and threshold
230 potentials, faster AP upstrokes, and narrower and smaller APs. These effects are most
231 pronounced in homozygous animals, with intermediate or minimal changes in heterozygotes. As
232 the WT PV population includes neurons that do not express *Kcng4*, the comparison of
233 heterozygous and homozygous animals directly assesses differences among neurons that would
234 typically express *Kcng4*, thereby confirming that alterations in the AP waveform reflect loss of
235 *Kcng4* rather than variability between PV subclasses or differences in mouse genetic
236 background. Thus, Kv6.4 shapes AP waveform in PV neurons. Notably, these alterations do not
237 result in a higher firing frequency but rather appear to refine the response of PV neurons during
238 periods of high activity.
239
240 **Kv6.4 regulates paired-pulse depression at PV-PYR synapses during high-frequency AP**
241 **firing**
242
243 To study the consequences of Kv6.4 ablation on inhibitory synapses, we performed paired whole-
244 cell recordings in L2/3 PV neurons and connected PYR neurons (**Fig. 4*A***). This analysis included
245 wildtype (n=11/9 pairs/mice) and homozygous (n=10/8 pairs/mice) groups. We evoked action
246 potentials in PV neurons by current injection under current-clamp and simultaneously measured
247 the resulting inhibitory postsynaptic currents (IPSCs) in neighboring PYR neurons under voltage-
248 clamp (**Fig. 4*B***). Excitatory currents were pharmacologically blocked. PYR neuron recordings
249 used a high-chloride cesium-based internal solution to amplify inhibitory currents, resulting in
250 inward GABAergic currents at resting membrane potentials. Synaptic currents were also
251 converted to conductance to isolate postsynaptic channel activation independent of recording
252 conditions (see ***Synaptic Properties*** in ***Materials and Methods***). We did not identify differences
253 in IPSC peak amplitude, whether assessed as current or conductance, or in the passive
254 properties (membrane resistance, membrane capacitance, or membrane time constant) of PYR
255 neurons between groups (**Fig. 4*C*** and **Dataset S3**).
256
257 We found that Kv6.4 modulates synaptic depression during high-frequency firing, as indicated by
258 altered inhibitory currents in response to paired-pulse stimulation. Specifically, we recorded
259 IPSCs in PYR neurons triggered by pairs of action potentials in PV neurons with varying
260 interstimulus intervals (Δt = 10, 20, 50, 100, 200, 500, 1000 ms; **Fig. 4*D***). The amplitude of
261 overlapping IPSCs was quantified by subtracting the residual decay of the first IPSC from the
262 peak of the second (see ***Synaptic Properties*** in ***Materials and Methods***). We observed that the

263 paired-pulse ratio of inhibition (PPR_i) and conductance (PPR_g) is significantly higher in mice that
264 lack Kv6.4 compared to control mice, but only at short interstimulus intervals, Δt = 10 ms (PPR_i:
265 WT/WT = 0.52 ± 0.031, Cre/Cre = 0.68 ± 0.035; unpaired two-tailed t-test, p = 0.003; PPR_g:
266 WT/WT = 0.52 ± 0.036, Cre/Cre = 0.69 ± 0.038; unpaired two-tailed t-test, p = 0.005) and Δt = 20
267 ms (PPR_i: WT/WT = 0.50 ± 0.036, Cre/Cre = 0.60 ± 0.016; p = 0.022; PPR_g: WT/WT = 0.48 ±
268 0.035, Cre/Cre = 0.57 ± 0.020; unpaired two-tailed t-test, p = 0.043) (**Fig. 4*E*** and **Dataset S3**).
269 This demonstrates that the probability of GABA release is lower in mice lacking *Kcng4*. Moreover,
270 the relationship between paired-pulse ratio and interstimulus interval was significantly different
271 between genotypes (repeated-measures ANOVA; current, p = 0.032; conductance, p = 0.038;
272 **Dataset S3**), indicating that synaptic depression varied across interstimulus intervals as a
273 function of Kv6.4 expression. Thus, paired-pulse depression is reduced at PV-PYR synapses in
274 the absence of Kv6.4 expression for presynaptic APs firing faster than ~50 Hz, which is well
275 below the maximal firing rates (hundreds of Hz) of cortical PV neurons *in vivo* (40).
276
277 We observed similar trends in the amplitude of inhibitory currents elicited by a 5-pulse train,
278 normalized to the first pulse: effects were only apparent at the shortest interstimulus interval (**Fig.**
279 **4 *F-H*** and **Dataset S3**). As the decay of preceding IPSCs was not corrected in the analysis of 5-
280 pulse train measurements (see ***Synaptic Properties*** in ***Materials and Methods***), the differences
281 between groups in this analysis may appear less pronounced than in the paired-pulse analysis. At
282 Δt = 10 ms, both current (WT/WT = 0.65 ± 0.025, Cre/Cre = 0.78 ± 0.051; unpaired two-tailed t-
283 test, p = 0.022) and conductance (WT/WT = 0.61 ± 0.027, Cre/Cre = 0.76 ± 0.059; unpaired two-
284 tailed t-test, p = 0.035) were significantly higher for the third pulse in homozygous mice. No
285 differences were detected for other pulses or interstimulus intervals in individual comparisons,
286 and repeated-measures ANOVA across all five pulses revealed no significant overall effect of
287 genotype, although a trend toward higher normalized amplitudes in the absence of Kv6.4 was
288 observed at the shortest interstimulus interval (**Fig. 4 *G-H***, **Fig. S*6***, and **Dataset S3**).
289
290 Together, these results demonstrate that Kv6.4 selectively tunes synaptic depression at PV-PYR
291 synapses during high-frequency activity, without influencing steady-state inhibition or IPSCs at
292 longer interstimulus intervals. These data reveal a function for Kv6.4 in regulating the precision of
293 inhibitory signaling at cortical PV-PYR synapses under fast-spiking conditions.
294
295 **Discussion**
296
297 Our findings reveal that Kv6.4 expression shapes both the intrinsic properties and synaptic output
298 of PV neurons during high-frequency firing. Kv6.4 depolarizes the interspike potential and
299 broadens the AP waveform in PV neurons, which we propose subsequently elevates the initial
300 probability of GABA release at PV-PYR cell synapses, resulting in the enhanced paired-pulse
301 depression observed (**Fig. 5**). Subtle alterations in AP waveform, and consequently in
302 presynaptic Ca^{2+} entry, are known to exert supralinear effects on postsynaptic current amplitude
303 (41–43) underscoring the sensitivity of release to AP narrowing or broadening. In PV neurons,
304 Ca^{2+}channels and GABA release are tightly coupled to rapidly translate changes in AP waveform
305 into graded inhibition (11). Deletion of both *Kcng4* alleles results in a ~10% change in AP width
306 (**Dataset S2**) but a ~30% change in paired-pulse ratio (**Dataset S3**). This ~3-fold amplification of
307 Kv6.4-dependent effects is expected if AP broadening is also present in the presynaptic boutons
308 of PV neurons. Kv3 channels have long been recognized as the primary regulators of rapid firing
309 in PV neurons and synaptic depression at PV-PYR synapses through AP narrowing (22, 44). We
310 demonstrate that a silent ion channel subunit engages these dynamics to modulate PV inhibition
311 in a firing-frequency-dependent manner, a mechanism that is particularly relevant to fast-spiking
312 interneurons.
313
314 The effects of Kv6.4 are likely mediated through its interactions with Kv2 subunits. The broader
315 expression pattern of Kv2.1 supports regulation of excitability across cell types, whereas the
316 selective enrichment of Kv6.4 in PV neurons enables precise, cell-type-specific control of

317 inhibitory output during high-frequency firing. The altered interspike potential observed in Kv6.4
318 knock-out neurons is consistent with prior findings that Kv6.4 subunits influence the inactivation
319 properties of Kv2 heterotetramers (29, 30, 32–35). Kv2 current provides repolarizing drive that
320 accumulates during high-frequency trains due to its slow kinetics, preventing AP broadening (28,
321 45, 46). Loss of Kv2.1 prolongs APs and broadens Ca^{2+} transients specifically during high-
322 frequency firing (45). In line with this, Kv6.4 broadens APs in PV neurons likely by reducing Kv2
323 current density, as it promotes the inactivation of its Kv2 partners during repolarization (29, 30).
324 Kv6.4 is therefore expected to share Kv2 subcellular localization patterns, forming clusters at the
325 somatodendritic membrane (45, 46). The recent availability of effective Kv6.4 antibodies (36) will
326 enable direct assessment of its localization in PV neurons.
327
328 Altered repolarization dynamics likely emerge at the interspike potential and accumulate during
329 repetitive firing, progressively modifying the AP waveform, reducing its duration, amplitude, and
330 threshold while increasing upstroke velocity. These waveform changes are expected to modify
331 synaptic release properties during high-frequency firing, consistent with our observation of altered
332 paired-pulse ratios at short interstimulus intervals. The influence of Kv6.4 likely accompanies
333 secondary effects to other potassium and sodium channels that further influence the spike train
334 (47). Thus, Kv6.4 regulates PV inhibition onto pyramidal neurons in a frequency-dependent
335 manner, which is consistent with its formation of channel complexes with Kv2 subunits.
336
337 ***Kcng4*+ as a functional PV subclass in cortical development and plasticity**
338
339 We find that the Kv6.4 silent subunit is selectively enriched in mature PV neurons—
340 with minimal expression in other cortical cell types aside from astrocytes—and is restricted to a
341 distinct transcriptional supertype of PV neurons (10). This specificity distinguishes Kv6.4 from
342 broadly expressed potassium channels, such as Kv2.1 or Kv3.1 (3), making it an attractive
343 candidate for selective targeting of this PV subclass. *Kcng4* has been identified as a marker of a
344 PV subclass in the GPe (37), where *Kcng4*+ neurons were implicated in motor pattern regulation,
345 but their physiological properties had not been defined. Here, we link this molecularly defined PV
346 supertype to distinct physiological properties. Recent efforts in the molecular targeting of
347 inhibitory neuron types have advanced our ability to dissect and manipulate circuit function across
348 species (48). Kv6.4 thus represents a molecular marker of a specialized PV subclass with
349 previously uncharacterized physiological roles, offering a new axis for selective circuit
350 interrogation and tool development.
351
352 Kv6.4 expression confers a frequency-dependent mechanism for modulating PV output, which
353 may facilitate adaptive changes in cortical circuits given that PV neurons form dense, nonspecific
354 wiring with PYR neurons (49). *Kcng4* expression broadly parallels the spatiotemporal pattern of
355 *Pvalb* but is particularly enriched in S1 L4, where sensory inputs first reach somatosensory cortex
356 (50) and where inhibition mediates experience-dependent plasticity during critical periods (17,
357 50). The onset of Kv6.4 expression may also influence early sensory-driven plasticity (50).
358 Indeed, PV-mediated experience-dependent plasticity in S1 is regulated by potassium channel
359 function (18) and transcription (26). The role of Kv6.4 may be particularly relevant to motor and
360 sensory learning, as we and others have found that Kv6.4 is enriched in mouse motor and
361 sensory areas (36) and is involved in sensing pain (32, 34, 35). Thus, Kv6.4 could link short-term
362 synaptic plasticity with long-term learning, and disruptions in its function could interfere with
363 cortical excitation-inhibition, plasticity, and development.
364
365 **Pathophysiological implications of Kv6.4 dysfunction**
366
367 Cortical circuit dysfunction in developmental and neurodegenerative disorders often arises from
368 dysregulation of ion channels and GABAergic inhibition. Several voltage-gated ion channels and
369 their regulators have been implicated in autism spectrum disorder, epilepsy, intellectual disability,
370 and Alzheimer's disease, such as the voltage-gated sodium channels Nav1.1 and Nav1.2 (48,

51), the synaptic adhesion molecule Cntnap4 (52), the Kv3 channel family (53), and NRG1-ErbB4 signaling that modulates Kv1.1 channels (25). These mechanisms operate within defined developmental windows or neuronal populations, such as PV neurons, to regulate excitability, plasticity, and network stability, and the disruption of these functions can result in abnormal sensory processing and cognitive deficits.

Kv6.4 has recently emerged as a clinically relevant modulator of neuronal excitability, motivating further investigation into its role in PV neurons *in vivo*. Loss-of-function *Kcng4* mutations in humans have been associated with reduced pain sensitivity in migraine (28, 34, 35) and labor during pregnancy (32), likely due to altered function of Kv2.1/Kv6.4 heterotetramers and disrupted excitability. Kv2.1/Kv6.4 complexes exhibit reduced sensitivity to channel blockers compared with Kv2.1 alone (33), and new pharmacological tools can distinguish silent Kv subunits from standard delayed rectifiers (54). These approaches can be leveraged to identify and target Kv6.4-containing complexes for functional or therapeutic studies. Complete Kv6.4 loss is poorly tolerated, as homozygous mutations are associated with male sterility (55) and hydrocephalus (56) in mice, suggesting that dosage-sensitive or cell-type-specific approaches may be necessary for potential interventions. Mutations in Kv2 channels resulting in complete or partial channel loss-of-function are linked to epilepsy and neurodevelopmental disorders such as autism spectrum disorder and intellectual disability, marked by seizures, motor and language problems, behavioral deficits, and ataxia (28, 57–60). Homozygous *Kcnb1* deletion in mice results in hippocampal hyperexcitability, epileptiform activity, accelerated seizure progression, locomotor hyperactivity, and impaired spatial learning (61). Future studies could examine how Kv6.4/Kv2.1 heterotetramers govern the timing and strength of PV-mediated inhibition during sensory processing and learning *in vivo*, and how these mechanisms are disrupted in disease.

Materials and Methods

Mice

We used Kcng4^{Cre} (The Jackson Laboratory, RRID:IMSR_JAX:029414) and PV^{Cre} (The Jackson Laboratory, RRID:IMSR_JAX:017320) mouse lines in this study. Both lines were crossed to the Ai14 reporter line (The Jackson Laboratory, RRID:IMSR_JAX:007914) to fluorescently label cells with tdTomato following Cre-mediated recombination. All Ai14 reporter animals (B6.Cg background) were heterozygous for the Ai14 allele. Kcng4^{Cre} (B6.129(SJL) background) is a knock-in/knock-out line in which Cre recombinase is inserted into exon 2 of the *Kcng4* gene, disrupting endogenous *Kcng4* gene expression. Kcng4^{Cre} animals used in this study were heterozygous (Kcng4$^{Cre/WT}$) or homozygous (Kcng4$^{Cre/Cre}$) for the Cre allele in addition to carrying one allele of Ai14. PV^{Cre} (B6.129P2 background) is a knock-in line in which Cre recombinase is inserted downstream of the *Pvalb* gene, without disrupting endogenous *Pvalb* gene expression. PV^{Cre} animals used in this study were heterozygous for the Cre allele (PV$^{Cre/WT}$) in addition to carrying one allele of Ai14. These animals, which retain two copies of *Kcng4*, were used as wildtype control mice with labelling of PV neurons for experiments that require PV neuron identification (e.g. whole-cell patch-clamp recordings). Additionally, we used C57BL/6J mice (The Jackson Laboratory, RRID:IMSR_JAX:000664) as wildtype control mice and for backcrossing.

We used mice between 2 and 20 weeks of age, with approximately balanced sex ratios. Mice were maintained on a 12h light/dark cycle under standard housing conditions. All experiments were performed in accordance with protocols approved by the Harvard Standing Committee on Animal Care (Protocol #: IS00000571-6), following guidelines described in the US NIH Guide for the Care and Use of Laboratory Animals.

Fluorescent RNA in situ hybridization

Wildtype mice (5-7 weeks old) were anesthetized with isoflurane, and brains were rapidly extracted and embedded in freezing media (Tissue-Tek O.C.T. Compound) on dry ice. Fresh-frozen brains were cryosectioned at 20 µm thickness (Leica CM3050S), adhered to SuperFrost Plus glass slides (VWR), and immediately refrozen, with short-term sample storage at -20°C and long-term sample storage at -80°C. Multiplexed fluorescent RNA in situ hybridization (FISH) was performed using the RNAscope Reagent Kit v2 (Advanced Cell Diagnostics, ACD) in collaboration with the Harvard Medical School Neurobiology Imaging Facility. The tissue was processed according to manufacturer instructions using a Protease III treatment for 30 min at room temperature. The following probes were used: Mm-*Pvalb* (ACD 421931), Mm-*Kcng4* (ACD 316931-C2), and Mm-*Kcnb1* (ACD 316941-C3). Samples were validated using positive and negative control probes, and nuclei were counterstained with DAPI. Samples were then imaged on an Olympus VS200 slide scanning microscope using a 20x objective and a Leica Stellaris 8 confocal microscope with a 63x oil-immersion objective. ROIs were drawn manually and quantified using QuPath, with further analysis in MATLAB (R2024a).

Histology

Mice (2-20 weeks old) were anesthetized with isoflurane and transcardially perfused with 4% paraformaldehyde (PFA) in phosphate-buffered saline (PBS). Brains were dissected and postfixed in 4% PFA overnight at 4°C and transferred to 30% sucrose for at least 1 day prior to cryosectioning. Brains were embedded in freezing media (Tissue-Tek O.C.T. Compound), coronally sectioned at 50 µm thickness (Leica CM3050S), and stored in PBS at 4°C. Sections were stained with DAPI (Sigma-Aldrich D9542) for 10 minutes at room temperature, mounted on SuperFrost Plus glass slides (VWR), and coverslipped with mounting medium (ProLong™ Gold Antifade Mountant). Samples were imaged on an Olympus VS200 slide scanning microscope using a 20x objective and a Leica Stellaris 8 confocal microscope with a 63x oil-immersion objective.

Acute slice preparation

Mice (5-7 weeks old) were anesthetized with isoflurane and immediately decapitated following transcardial perfusion with ice-cold artificial cerebral spinal fluid (ACSF) containing (in mM): 125 NaCl, 2.5 KCl, 25 $NaHCO_3$, 2 $CaCl_2$, 1 $MgCl_2$, 1.25 NaH_2PO_4, and 17 glucose (300–310 mOsm kg^{-1}). Extracted brains were transferred to a Leica VT1200s vibratome for preparation of 300 µm coronal slices in ice-cold ACSF. After cutting, slices were incubated for 3–6 min in choline-based solution at 34°C containing (in mM): 110 choline chloride, 25 $NaHCO_3$, 2.5 KCl, 7 $MgCl_2$, 0.5 $CaCl_2$, 1.25 NaH_2PO_4, 25 glucose, 11.6 ascorbic acid, and 3.1 pyruvic acid (320–330 mOsm kg^{-1}). In a second chamber, slices were incubated in ACSF at 34°C for 1 h. The slices were then cooled to room temperature (> 1h) and maintained until electrophysiology recordings were performed. All solutions were continuously bubbled with carbogen gas (95% O_2, 5% CO_2).

Whole-cell patch-clamp recordings were conducted in L2/3 of primary somatosensory cortex (S1) in artificial cerebrospinal fluid (ACSF) at 30–32°C with a perfusion rate of 4–6 mL min^{-1}. Layer 2/3 was defined as spanning from 100–200 µm to 400–500 µm below pia. tdTomato+ neurons were identified using a Scientifica microscope equipped with a digital camera (Hamamatsu), an epifluorescence LED light source (CoolLED), and a 60x/0.9NA LUMPlanFl/IR water-immersion objective (Olympus). Patch pipettes were pulled from borosilicate glass (Sutter Instruments) with resistances of 2.0–3.5 MΩ. Recordings were performed using a Multiclamp 700B amplifier (Molecular Devices) and a data acquisition board (National Instruments). Data were collected and analyzed using MATLAB custom-written software (ScanImage) and scripts (R2023a).

Intrinsic properties

For whole-cell current-clamp recordings assessing intrinsic properties, patch pipettes were filled with low chloride potassium-based internal solution (in mM): 135 $KMeSO_3$, 3 KCl, 10 HEPES, 1 EGTA, 0.1 $CaCl_2$, 4 Mg-ATP, 0.3 Na-GTP, and 8 Na_2Phosphocreatine (pH 7.3 adjusted with KOH, 290–300 mOsm kg^{-1}). The following synaptic blockers were bath-applied: NBQX (10 μM, Tocris), CPP (10 μM, Tocris), and SR 95531 hydrobromide (10 μM, Tocris). Signals were filtered at 10 kHz and digitized at 50 kHz.

The experimenter was blinded to heterozygous (Kcng4$^{Cre/WT}$; Ai14) and homozygous (Kcng4$^{Cre/Cre}$; Ai14) genotypes, and age-matched littermates were used. Neuronal responses were measured to current steps delivered at both (1) the neuron's endogenous resting membrane potential and (2) at -70 mV maintained via continuous current injection. Resting membrane potential was measured shortly after breaking in, after which all other intrinsic properties were measured. Action potential threshold was defined as the membrane potential at which the dV/dt exceeded 4% of the maximum slope during the upstroke.

No series resistance compensation was used. Series resistance did not exceed 20 MΩ. As provided in **Dataset S1**, mean resting membrane potential was -74.65 ± 1.02 mV, mean series resistance was 11.11 ± 0.40 MΩ, and mean membrane resistance was 71.14 ± 5.94 MΩ for *Pvalb*$^{Cre/WT}$ animals; -74.09 ± 1.36 mV, 11.18 ± 0.56 MΩ, and 67.37 ± 5.86 MΩ for Kcng4$^{Cre/WT}$ animals; and -73.55 ± 0.88 mV, 10.71 ± 0.36 MΩ, and 63.94 ± 5.78 MΩ for Kcng4$^{Cre/Cre}$ animals.

Synaptic properties

For whole-cell voltage-clamp recordings assessing synaptic properties, patch pipettes were filled with high chloride cesium-based internal solution (in mM): 125 CsCl, 10 TEA-Cl, 10 HEPES, 0.1 EGTA, 3.3 QX-314, 1.8 $MgCl_2$, 4 Mg-ATP, 0.3 Na-GTP, and 8 Na_2Phosphocreatine (pH 7.3 adjusted with CsOH, 290–300 mOsm kg^{-1}). The following synaptic blockers were bath-applied: NBQX (10 μM, Tocris) and CPP (10 μM, Tocris). Signals were filtered at 10 kHz and digitized at 10 kHz.

Cells in PV-PYR pairs were typically < 50 μm apart. Action potentials were evoked in PV neurons at the minimal current injection required between 1–2 nA (1 ms) to elicit a postsynaptic current in the PYR neuron. Absolute amplitude was measured shortly after breaking in via 3-5 single action potential stimulation pulses. Afterwards, eleven distinct action potential stimulation patterns were applied, each of which was repeated 3–5 times per paired recording in a randomized order. For analysis of paired-pulse recordings, overlap between the first and second IPSCs was corrected by subtracting the residual decay of the first IPSC from the peak of the second IPSC. No correction was applied to 5-pulse trains.

Again, no series resistance compensation was used during the experiment. Series resistance did not exceed 30 MΩ. For all paired recordings, holding current did not exceed 200 pA at −70 mV. Mean series resistance was 18.93 ± 0.90 MΩ and mean membrane resistance was 210.90 ± 20.50 MΩ for PYR neurons recorded from *Pvalb*$^{Cre/WT}$ animals; mean series resistance was 20.40 ± 1.51 MΩ and mean membrane resistance was 204.11 ± 11.80 MΩ for PYR neurons recorded from Kcng4$^{Cre/Cre}$ animals.

IPSC peak amplitude was converted to conductance according to established procedures to compensate for variability in parameters such as series resistance and membrane resistance (62). Given that we are only measuring inhibitory current $g_i(t)$ and there is no excitatory current $g_e(t)$:

$$g_{syn}(t) = g_e(t) + g_i(t) = g_i(t)$$

We used the following three equations to solve for $g_i(t)$:

$$I_i(t) = g_i(t)[V(t) - E_i(t)] \quad (1)$$

$$V(t) = V_{hold} - I(t)R_{series} \quad (2)$$

$$I(t) = I_i(t) + \frac{[V(t) - E_{rest}]}{R_{membrane}} \quad (3)$$

We derived the following equation for $g_i(t)$:

$$g_i(t) = \frac{E_{rest}}{R_{membrane}(V_{hold} - I(t)R_{series} - E_i)} \quad (4)$$

We measured $R_{membrane}$ and R_{series} from a test pulse during the recording, and we separately measured E_{rest} (–16 mV) and E_i (–2.5 mV). The PV neuron was held at -70 mV; thus V_{hold} = –70 mV. Using these parameters, we converted inhibitory current I(t) to conductance $g_i(t)$.

Quantification and statistical analysis

Data is plotted as mean ± SEM. P values are represented as * for P < 0.05 and ** P < 0.01, and details regarding the *p* values and statistical tests are provided in the figure legends and supplementary files.

Data, materials, and software availability

All study data are included in the article and/or SI Appendix. The original code reported in this paper will be publicly available at the time of publication on GitHub [link will be provided]. Any additional information regarding the data and analysis is available from the lead contact upon request.

Acknowledgments

We thank all members of the Sabatini lab for helpful advice and technical assistance. We are grateful to W. Wang for advice on electrophysiology experiments. We thank C. King for mouse colony management and assistance with blinding the experimenter to mouse genotypes. We also thank C. Chen, W. Regehr, G. Fishell, and M. Andermann for useful insights. Additionally, we thank M. Ocana, M. EL-Rifai, and the Neurobiology Imaging Facility at Harvard Medical School for collaborating with our lab to complete the FISH experiments. We are especially grateful to M. Sherman, J. Wallace, W. Wang, T. Kula, J. McMahon, S. Liu, A. Girasole, and K. Mastro for feedback on the manuscript.

This work was supported by NIH R35NS137336 (to B.L.S), National Science Foundation Graduate Research Fellowship Program (NSF-GRFP) (to S.G.) and the Herchel Smith Graduate Fellowship (to S.G.).

584 **References**
585

586 1. E. S. Lein, *et al.*, Genome-wide atlas of gene expression in the adult mouse brain. *Nature* **445**,
587 168–176 (2007).

588 2. B. Tasic, *et al.*, Adult mouse cortical cell taxonomy revealed by single cell transcriptomics. *Nat.*
589 *Neurosci.* **19**, 335–346 (2016).

590 3. S. Hrvatin, *et al.*, Single-cell analysis of experience-dependent transcriptomic states in the
591 mouse visual cortex. *Nat Neurosci* **21**, 120–129 (2018).

592 4. B. Tasic, *et al.*, Shared and distinct transcriptomic cell types across neocortical areas. *Nature*
593 **563**, 72–78 (2018).

594 5. A. Saunders, *et al.*, Molecular Diversity and Specializations among the Cells of the Adult
595 Mouse Brain. *Cell* **174**, 1015-1030.e16 (2018).

596 6. V. Kozareva, *et al.*, A transcriptomic atlas of mouse cerebellar cortex comprehensively defines
597 cell types. *Nature* **598**, 214–219 (2021).

598 7. Z. Yao, *et al.*, A taxonomy of transcriptomic cell types across the isocortex and hippocampal
599 formation. *Cell* **184**, 3222-3241.e26 (2021).

600 8. Z. Yao, *et al.*, A transcriptomic and epigenomic cell atlas of the mouse primary motor cortex.
601 *Nature* **598**, 103–110 (2021).

602 9. J. Langlieb, *et al.*, The molecular cytoarchitecture of the adult mouse brain. *Nature* **624**, 333–
603 342 (2023).

604 10. M. Zhang, *et al.*, Molecularly defined and spatially resolved cell atlas of the whole mouse
605 brain. *Nature* **624**, 343–354 (2023).

606 11. H. Hu, J. Gan, P. Jonas, Fast-spiking, parvalbumin+ GABAergic interneurons: From cellular
607 design to microcircuit function. *Science* **345**, 1255263 (2014).

608 12. B. V. Atallah, W. Bruns, M. Carandini, M. Scanziani, Parvalbumin-Expressing Interneurons
609 Linearly Transform Cortical Responses to Visual Stimuli. *Neuron* **73**, 159–170 (2012).

610 13. N. R. Wilson, C. A. Runyan, F. L. Wang, M. Sur, Division and subtraction by distinct cortical
611 inhibitory networks in vivo. *Nature* **488**, 343–348 (2012).

612 14. M. Xue, B. V. Atallah, M. Scanziani, Equalizing excitation–inhibition ratios across visual
613 cortical neurons. *Nature* **511**, 596–600 (2014).

614 15. F. Pouille, M. Scanziani, Enforcement of Temporal Fidelity in Pyramidal Cells by Somatic
615 Feed-Forward Inhibition. *Science* **293**, 1159–1163 (2001).

616 16. J. A. Cardin, *et al.*, Driving fast-spiking cells induces gamma rhythm and controls sensory
617 responses. *Nature* **459**, 663–667 (2009).

618 17. A. Maffei, K. Nataraj, S. B. Nelson, G. G. Turrigiano, Potentiation of cortical inhibition by
619 visual deprivation. *Nature* **443**, 81–84 (2006).

620 18. M. A. Gainey, J. W. Aman, D. E. Feldman, Rapid Disinhibition by Adjustment of PV Intrinsic
621 Excitability during Whisker Map Plasticity in Mouse S1. *J Neurosci* **38**, 4749–4761 (2018).

622 19. T. K. Hensch, Critical period plasticity in local cortical circuits. *Nat. Rev. Neurosci.* **6**, 877–888
623 (2005).

624 20. O. Marín, Interneuron dysfunction in psychiatric disorders. *Nat. Rev. Neurosci.* **13**, 107–120
625 (2012).

626 21. A. Erisir, D. Lau, B. Rudy, C. S. Leonard, Function of Specific K+ Channels in Sustained
627 High-Frequency Firing of Fast-Spiking Neocortical Interneurons. *J. Neurophysiol.* **82**, 2476–2489
628 (1999).

629 22. B. Rudy, C. J. McBain, Kv3 channels: voltage-gated K+ channels designed for high-frequency
630 repetitive firing. *Trends Neurosci.* **24**, 517–526 (2001).

631 23. C.-C. Lien, P. Jonas, Kv3 Potassium Conductance is Necessary and Kinetically Optimized for
632 High-Frequency Action Potential Generation in Hippocampal Interneurons. *J. Neurosci.* **23**, 2058–
633 2068 (2003).

634 24. E. M. Goldberg, *et al.*, K+ Channels at the Axon Initial Segment Dampen Near-Threshold
635 Excitability of Neocortical Fast-Spiking GABAergic Interneurons. *Neuron* **58**, 387–400 (2008).

636 25. K.-X. Li, *et al.*, Neuregulin 1 regulates excitability of fast-spiking neurons through Kv1.1 and
637 acts in epilepsy. *Nat. Neurosci.* **15**, 267–273 (2012).

638 26. N. Dehorter, *et al.*, Tuning of fast-spiking interneuron properties by an activity-dependent
639 transcriptional switch. *Science* **349**, 1216–1220 (2015).

640 27. E. Bocksteins, D. J. Snyders, Electrically Silent Kv Subunits: Their Molecular and Functional
641 Characteristics. *Physiology* **27**, 73–84 (2012).

642 28. E. Bocksteins, Kv5, Kv6, Kv8, and Kv9 subunits: No simple silent bystanders. *J. Gen. Physiol.*
643 **147**, 105–125 (2016).

644 29. E. Bocksteins, *et al.*, Conserved Negative Charges in the N-terminal Tetramerization Domain
645 Mediate Efficient Assembly of Kv2.1 and Kv2.1/Kv6.4 Channels*. *J Biol Chem* **284**, 31625–31634
646 (2009).

647 30. E. Bocksteins, A. J. Labro, D. J. Snyders, D. P. Mohapatra, The Electrically Silent Kv6.4
648 Subunit Confers Hyperpolarized Gating Charge Movement in Kv2.1/Kv6.4 Heterotetrameric
649 Channels. *Plos One* **7**, e37143 (2012).

650 31. E. Bocksteins, D. J. Snyders, M. Holmgren, Independent movement of the voltage sensors in
651 KV2.1/KV6.4 heterotetramers. *Sci. Rep.* **7**, 41646 (2017).

652 32. M. C. Lee, *et al.*, Human Labor Pain Is Influenced by the Voltage-Gated Potassium Channel
653 KV6.4 Subunit. *Cell Rep.* **32**, 107941 (2020).

654 33. L. Möller, G. Regnier, A. J. Labro, R. Blunck, D. J. Snyders, Determining the correct
655 stoichiometry of Kv2.1/Kv6.4 heterotetramers, functional in multiple stoichiometrical
656 configurations. *Proc. Natl. Acad. Sci.* **117**, 9365–9376 (2020).

657 34. G. Lacroix, S. Bhat, Z. Shafia, R. Blunck, KCNG4 Genetic Variant Linked to Migraine
658 Prevents Expression of KCNB1. *Int. J. Mol. Sci.* **25**, 8960 (2024).

659 35. D. Tewari, C. Sattler, K. Benndorf, Functional properties of a disease mutation for migraine in
660 Kv2.1/6.4 channels. *Biochem. Biophys. Res. Commun.* **738**, 150560 (2024).

661 36. T. A. Lacey, K. D. Murray, J. S. Trimmer, J. T. Sack, M. J. Ferns, Kv2/Kv6.4 Heteromeric
662 Potassium Channels Are Expressed in Spinal Motoneurons and Localized at C-Bouton
663 Synapses. *Eur. J. Neurosci.* **62**, e70243 (2025).

664 37. Q. Cui, *et al.*, Dissociable Roles of Pallidal Neuron Subtypes in Regulating Motor Patterns. *J*
665 *Neurosci* **41**, 4036–4059 (2021).

666 38. J.-P. David, J. I. Stas, N. Schmitt, E. Bocksteins, Auxiliary KCNE subunits modulate both
667 homotetrameric Kv2.1 and heterotetrameric Kv2.1/Kv6.4 channels. *Sci. Rep.* **5**, 12813 (2015).

668 39. Y. Kobayashi, Z. Ye, T. K. Hensch, Clock Genes Control Cortical Critical Period Timing.
669 *Neuron* **86**, 264–275 (2015).

670 40. B. Wang, *et al.*, Firing Frequency Maxima of Fast-Spiking Neurons in Human, Monkey, and
671 Mouse Neocortex. *Front. Cell. Neurosci.* **10**, 239 (2016).

672 41. B. L. Sabatini, W. G. Regehr, Control of Neurotransmitter Release by Presynaptic Waveform
673 at the Granule Cell to Purkinje Cell Synapse. *J. Neurosci.* **17**, 3425–3435 (1997).

674 42. J. G. G. Borst, B. Sakmann, Effect of changes in action potential shape on calcium currents
675 and transmitter release in a calyxtype synapse of the rat auditory brainstem. *Philos. Trans. R.*
676 *Soc. Lond. Ser. B: Biol. Sci.* **354**, 347–355 (1999).

677 43. J. R. P. Geiger, P. Jonas, Dynamic Control of Presynaptic Ca2+ Inflow by Fast-Inactivating
678 K+ Channels in Hippocampal Mossy Fiber Boutons. *Neuron* **28**, 927–939 (2000).

679 44. E. M. Goldberg, *et al.*, Specific Functions of Synaptically Localized Potassium Channels in
680 Synaptic Transmission at the Neocortical GABAergic Fast-Spiking Cell Synapse. *J Neurosci* **25**,
681 5230–5235 (2005).

682 45. J. Du, L. L. Haak, E. Phillips-Tansey, J. T. Russell, C. J. McBain, Frequency-dependent
683 regulation of rat hippocampal somato-dendritic excitability by the K+ channel subunit Kv2.1. *J.*
684 *Physiol.* **522**, 19–31 (2000).

685 46. H. Misonou, D. P. Mohapatra, J. S. Trimmer, Kv2.1: A Voltage-Gated K+ Channel Critical to
686 Dynamic Control of Neuronal Excitability. *NeuroToxicology* **26**, 743–752 (2005).

687 47. B. P. Bean, The action potential in mammalian central neurons. *Nat. Rev. Neurosci.* **8**, 451–
688 465 (2007).

689 48. D. Vormstein-Schneider, *et al.*, Viral manipulation of functionally distinct interneurons in mice,
690 non-human primates and humans. *Nat Neurosci* **23**, 1629–1636 (2020).

691 49. A. M. Packer, R. Yuste, Dense, Unspecific Connectivity of Neocortical Parvalbumin-Positive
692 Interneurons: A Canonical Microcircuit for Inhibition? *J. Neurosci.* **31**, 13260–13271 (2011).

693 50. D. E. Feldman, M. Brecht, Map Plasticity in Somatosensory Cortex. *Science* **310**, 810–815
694 (2005).

695 51. P. W. E. Spratt, *et al.*, The Autism-Associated Gene Scn2a Contributes to Dendritic
696 Excitability and Synaptic Function in the Prefrontal Cortex. *Neuron* **103**, 673-685.e5 (2019).

697 52. T. Karayannis, *et al.*, Cntnap4 differentially contributes to GABAergic and dopaminergic
698 synaptic transmission. *Nature* **511**, 236–240 (2014).

699 53. V. J. Olah, *et al.*, Biophysical Kv3 channel alterations dampen excitability of cortical PV
700 interneurons and contribute to network hyperexcitability in early Alzheimer's. *Elife* **11**, e75316
701 (2022).

702 54. R. G. Stewart, *et al.*, A Kv2 inhibitor combination reveals native neuronal conductances
703 consistent with Kv2/KvS heteromers. *eLife* **13**, RP99410 (2025).

704 55. G. Regnier, *et al.*, Targeted deletion of the Kv6.4 subunit causes male sterility due to
705 disturbed spermiogenesis. *Reprod., Fertil. Dev.* **29**, 1567 (2016).

706 56. H. Shen, E. Bocksteins, I. Kondrychyn, D. Snyders, V. Korzh, Functional antagonism of
707 voltage-gated K+ channel α-subunits in the developing brain ventricular system. *Development*
708 **143**, 4249–4260 (2016).

709 57. J. Jędrychowska, V. Korzh, Kv2.1 voltage-gated potassium channels in developmental
710 perspective. *Dev. Dyn.* **248**, 1180–1194 (2019).

711 58. C. G. F. de Kovel, *et al.*, Neurodevelopmental Disorders Caused by De Novo Variants in
712 KCNB1 Genotypes and Phenotypes. *JAMA Neurol.* **74**, 1228 (2017).

713 59. M. Kessi, *et al.*, Intellectual Disability and Potassium Channelopathies: A Systematic Review.
714 *Front. Genet.* **11**, 614 (2020).

715 60. N. M. Allen, S. Weckhuysen, K. Gorman, M. D. King, H. Lerche, Genetic potassium channel-
716 associated epilepsies: Clinical review of the Kv family. *Eur. J. Paediatr. Neurol.* **24**, 105–116
717 (2020).

718 61. D. J. Speca, *et al.*, Deletion of the Kv2.1 delayed rectifier potassium channel leads to
719 neuronal and behavioral hyperexcitability. *Genes, Brain Behav.* **13**, 394–408 (2014).

720 62. M. Wehr, A. M. Zador, Balanced inhibition underlies tuning and sharpens spike timing in
721 auditory cortex. *Nature* **426**, 442–446 (2003).

722

723

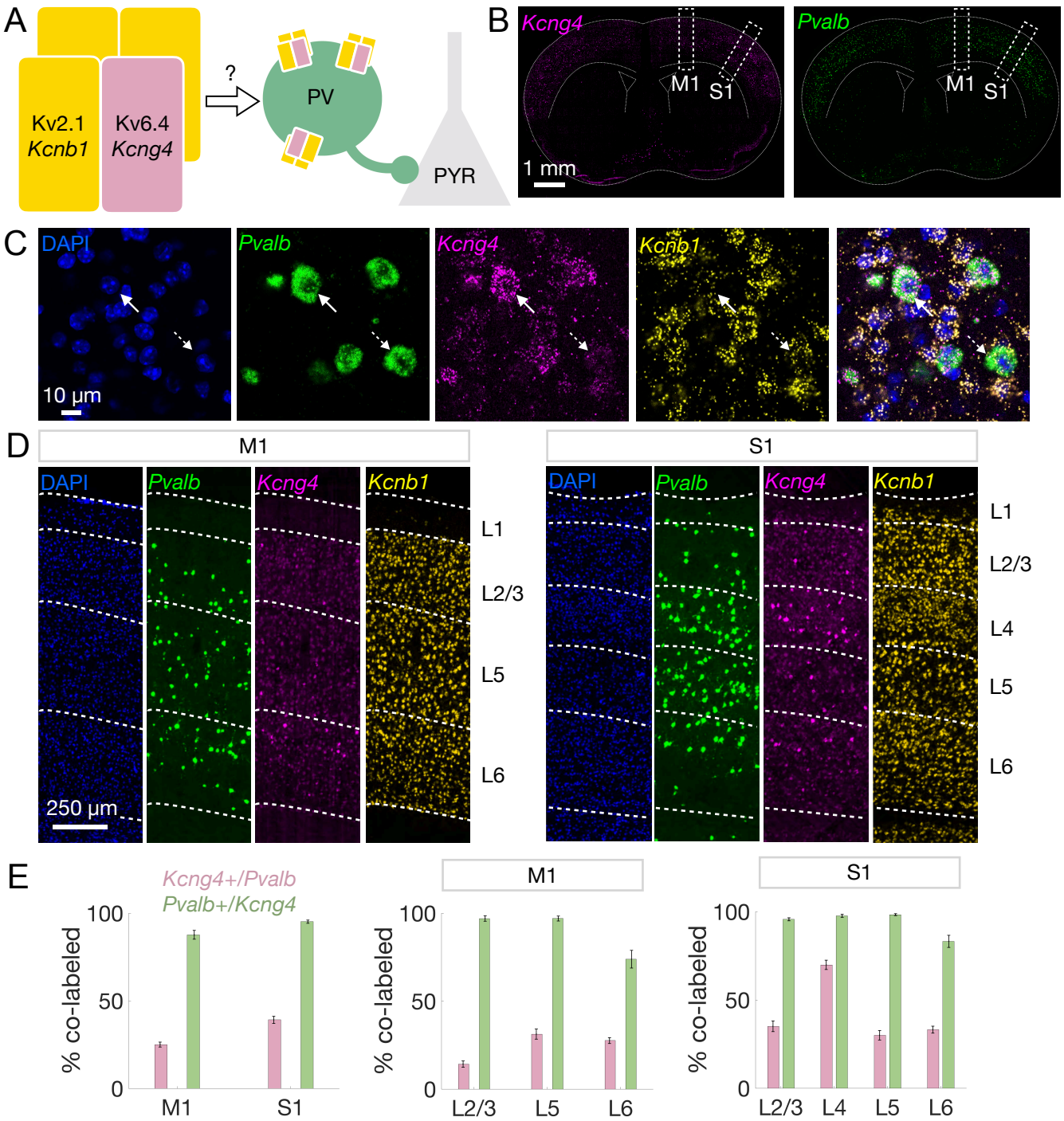
A
Kv2.1
Kcnb1
Kv6.4
Kcng4
?
PV
PYR
B
Kcng4
Pvalb
M1
S1
1 mm
C
DAPI
Pvalb
Kcng4
Kcnb1
10 µm
D
M1
S1
DAPI
Pvalb
Kcng4
Kcnb1
L1
L2/3
L4
L5
L6
250 µm
E
Kcng4+/Pvalb
Pvalb+/Kcng4
% co-labeled
100
50
0
M1
S1
L2/3
L4
L5
L6

Fig. 1. Cortical PV neurons selectively express *Kcng4*.
A, Schematic illustrating the hypothesis that Kv6.4 (encoded by *Kcng4*) confers cell-type-specific function by forming heterotetrameric channels with Kv2.1 (encoded by *Kcnb1*). We tested whether Kv6.4 modulates PV neuron excitability and PV inhibition of excitatory pyramidal (PYR) neurons.
B, Coronal brain sections displaying the spatial distribution of *Kcng4* (magenta, *left*) and *Pvalb* (green, *right*) mRNA across cortex detected by FISH. Subsequent analyses focus on primary motor (M1) and somatosensory (S1) cortical regions, indicated by white dashed boxes.
C, Representative images of individual cortical cells labeled with DAPI (blue) and FISH against *Pvalb* (green), *Kcng4* (magenta), and *Kcnb1* (yellow), followed by a merged view (*left* to *right*). Solid white arrows indicate a cell that co-expresses *Pvalb, Kcnb1,* and *Kcng4*, and dashed white arrows indicate a cell that co-expresses *Pvalb* and *Kcnb1*.
D, Representative images of M1 and S1 showing the spatial distribution of *Kcng4*, *Pvalb*, and *Kcnb1* mRNA. White dashed lines and text labels denote individual cortical layers (L).
E, Quantification of co-labeled cells displaying the percentage of *Pvalb*-expressing cells that are *Kcng4*+ (pink) and the percentage of *Kcng4*-expressing cells that are *Pvalb*+ (green) in M1 and S1 (n=6/18/36 mice/sections/hemispheres per region, 2-4 sections per mouse) across all layers (*left*). Quantification by cortical layer in M1 (*center*) and S1 (*right*).
Mean ± SEM displayed.

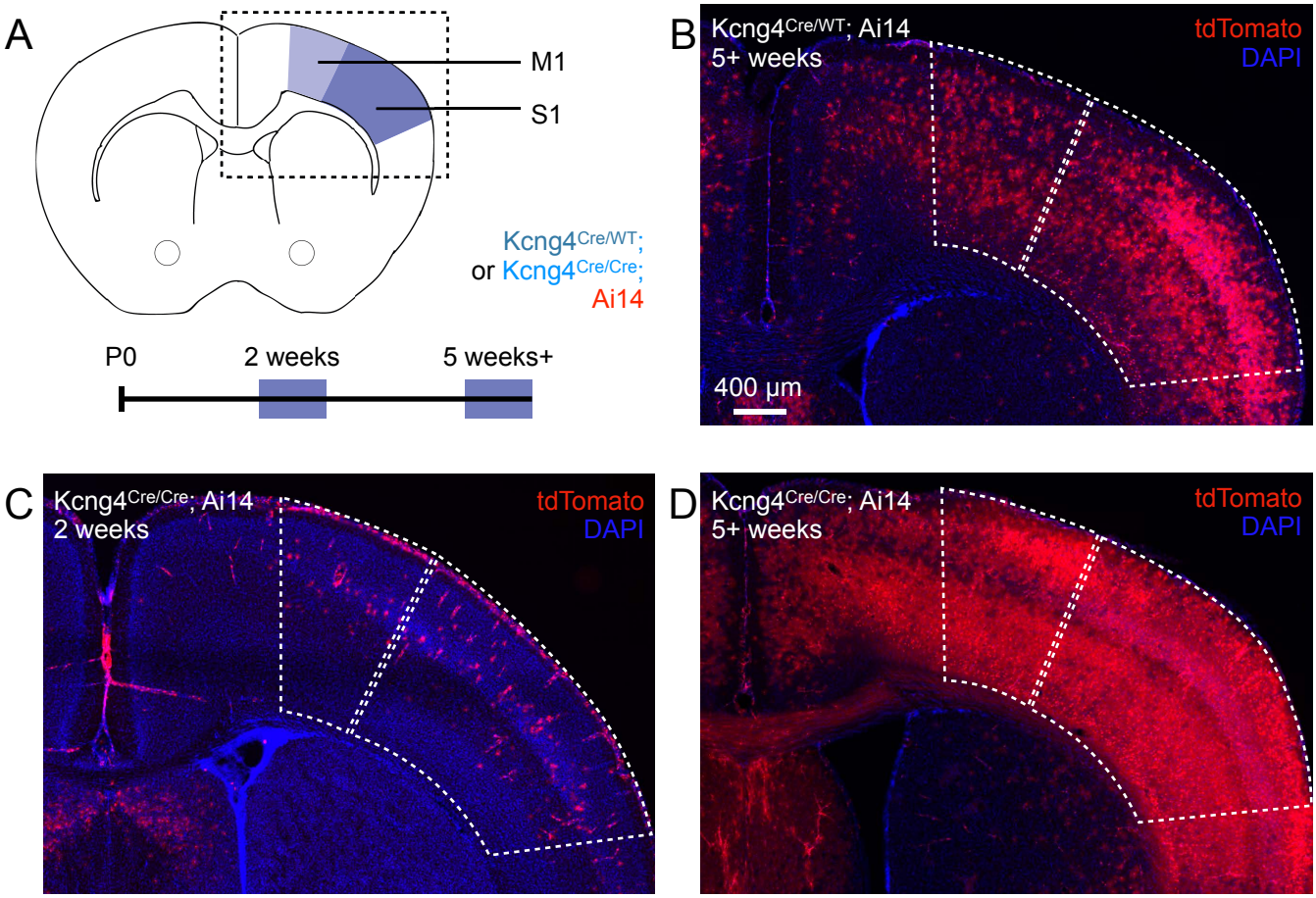
A
M1
S1
Kcng4Cre/WT;
or Kcng4Cre/Cre;
Ai14
P0
2 weeks
5 weeks+
B
Kcng4Cre/WT; Ai14
5+ weeks
tdTomato
DAPI
400 µm
C
Kcng4Cre/Cre; Ai14
2 weeks
tdTomato
DAPI
D
Kcng4Cre/Cre; Ai14
5+ weeks
tdTomato
DAPI

Fig. 2. Age dependence of Kcng4^{Cre} activation.
A, Schematic of the brain regions analyzed to assess Kcng4^{Cre} activation at juvenile (2 weeks) and adult (5+ weeks) timepoints in heterozygous (Kcng4$^{Cre/WT}$; Ai14) and homozygous (Kcng4$^{Cre/Cre}$; Ai14) mice. Analyses focused on primary motor (M1) and somatosensory (S1) cortex, as indicated.
B-D, Representative images showing tdTomato fluorescence in M1 and S1, as indicated in panel A, for Kcng4$^{Cre/WT}$; Ai14 mice at 5+ weeks **(B)**, and Kcng4$^{Cre/Cre}$; Ai14 mice at 2 weeks **(C)** and 5+ weeks **(D)**.

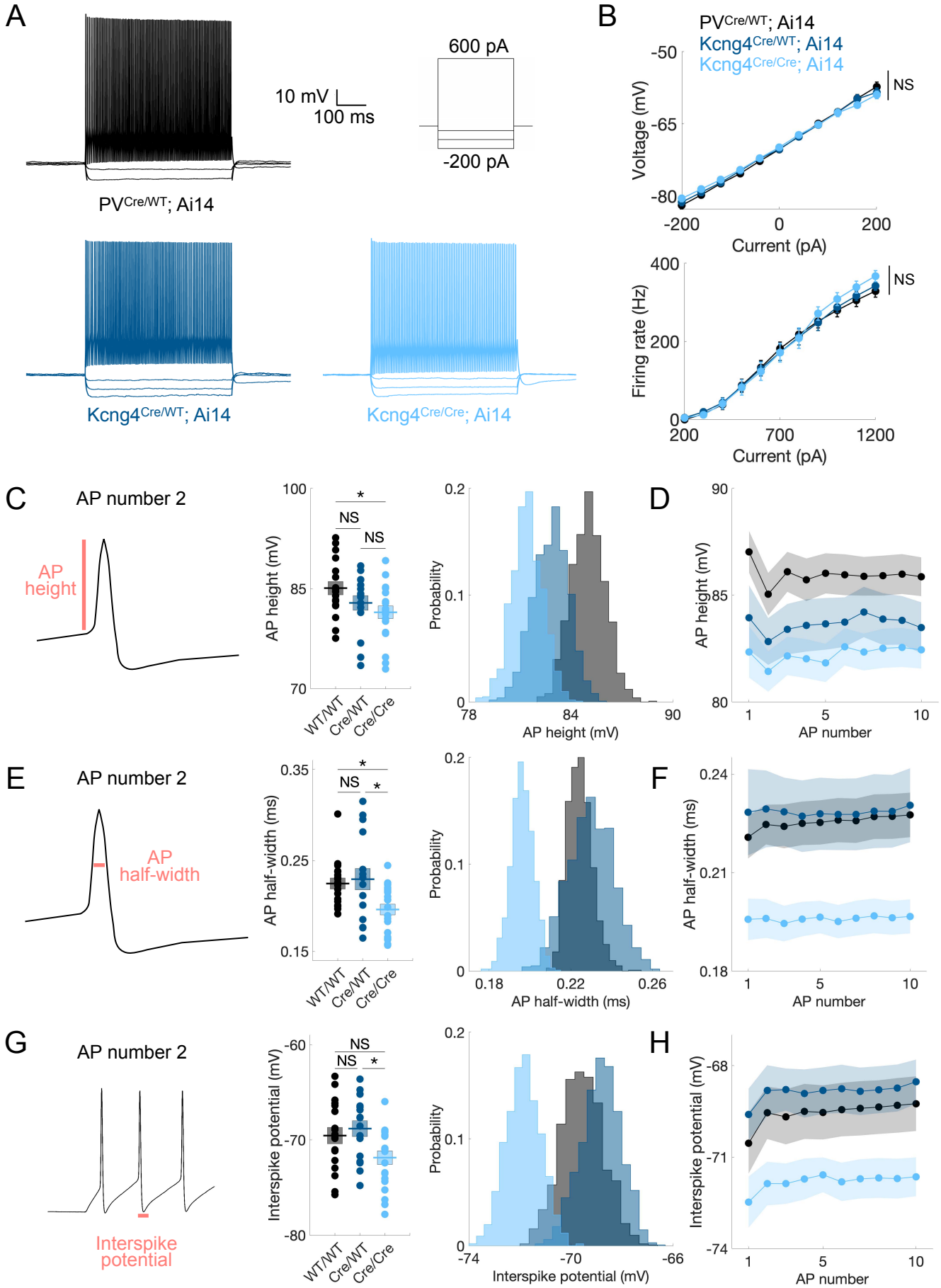
A
10 mV
100 ms
600 pA
-200 pA
PV$^{Cre/WT}$; Ai14
Kcng4$^{Cre/WT}$; Ai14
Kcng4$^{Cre/Cre}$; Ai14
B
PV$^{Cre/WT}$; Ai14
Kcng4$^{Cre/WT}$; Ai14
Kcng4$^{Cre/Cre}$; Ai14
Voltage (mV)
Current (pA)
NS
Firing rate (Hz)
Current (pA)
NS
C
AP number 2
AP height
AP height (mV)
WT/WT
Cre/WT
Cre/Cre
NS
NS
*
Probability
AP height (mV)
D
AP height (mV)
AP number
E
AP number 2
AP half-width
AP half-width (ms)
NS
*
*
Probability
AP half-width (ms)
F
AP half-width (ms)
AP number
G
AP number 2
Interspike potential
Interspike potential (mV)
NS
NS
*
Probability
Interspike potential (mV)
H
Interspike potential (mV)
AP number

Fig. 3. Kv6.4 modulates AP height, AP half-width, and interspike potential in PV neurons.
A, Representative whole-cell current-clamp recordings from L2/3 fast-spiking neurons in S1 of mice with two ($PV^{Cre/WT}$; Ai14), one ($Kcng4^{Cre/WT}$; Ai14), and no ($Kcng4^{Cre/Cre}$; Ai14) active alleles of *Kcng4*. Voltage responses to a series of current injections (–200, –120, –40, and 600 pA) are shown.
B, Voltage (mV, *top*) and firing rate (Hz, *bottom*) responses to stepwise current injections for wildtype (n=4/18 mice/cells), heterozygous (n=4/16), and homozygous (n=4/20) groups.
C, Schematic of action potential (AP) height (*left*) and its group mean measured for the 2nd AP (mV, *center*) in the first current step that elicited at least 10 APs. Bootstrapped distribution of the means (*right*).
D, Mean values across the first 10 APs (mV) in a response that elicited at least 10 APs.
E-H, As in **C** and **D** for AP half-width (ms*)* **(C)** and interspike potential (mV) **(D)**.
Mean ± SEM displayed. * $P < 0.05$; NS: not statistically significant. Repeated-measures ANOVA (Greenhouse-Geisser corrected) or one-way ANOVA (with Tukey-Kramer multiple comparisons). Bootstrapping (1,000 iterations) was used to visualize sample mean distributions.

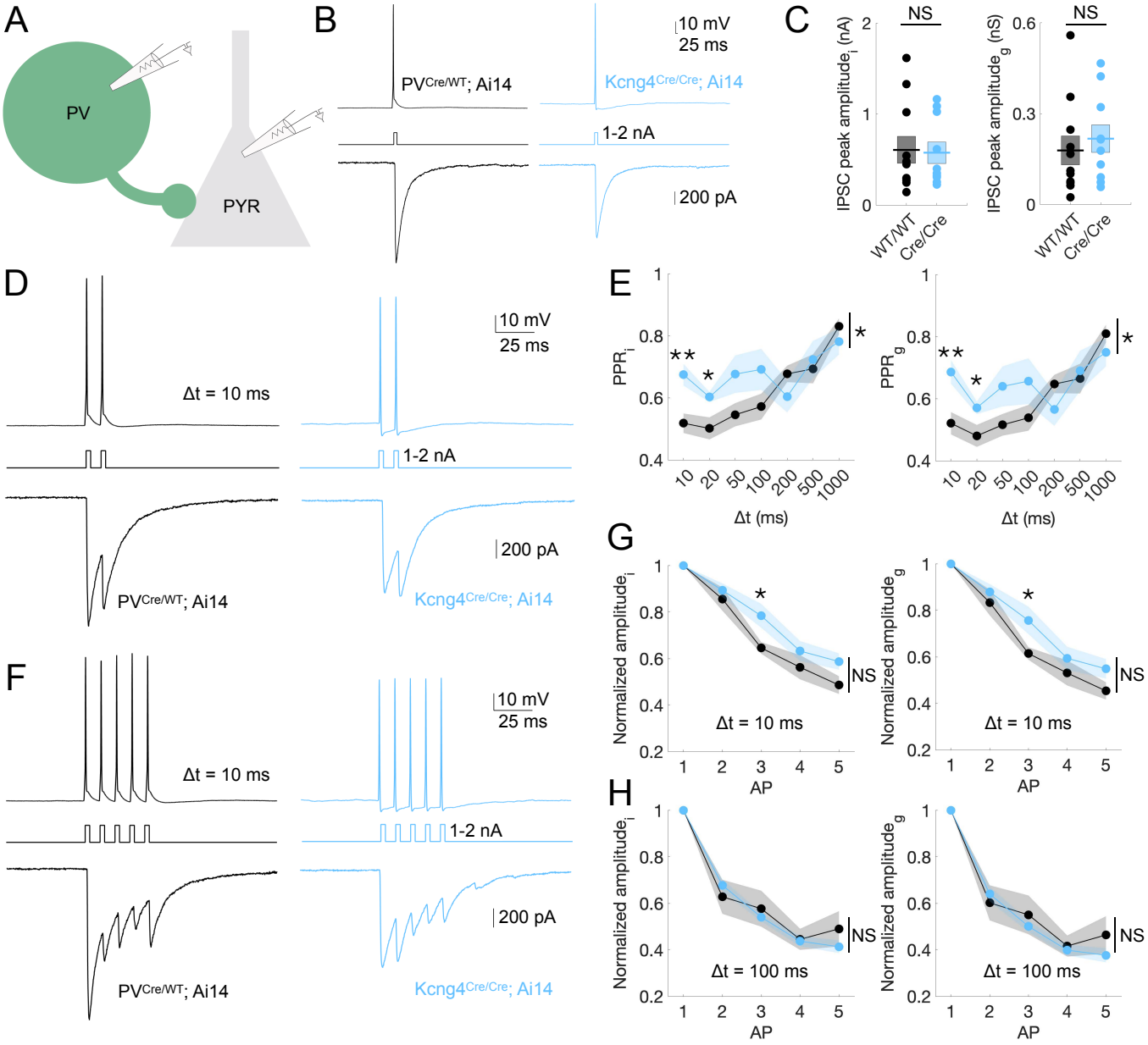
A
PV
PYR
B
PVCre/WT; Ai14
Kcng4Cre/Cre; Ai14
10 mV
25 ms
1-2 nA
200 pA
C
NS
IPSC peak amplitudei (nA)
IPSC peak amplitudeg (nS)
WT/WT
Cre/Cre
D
Δt = 10 ms
E
PPRi
PPRg
Δt (ms)
G
Normalized amplitudei
Normalized amplitudeg
AP
H
Δt = 100 ms

Fig. 4. Kv6.4 regulates paired-pulse depression at PV-PYR synapses during high-frequency AP firing.

A, Schematic of paired whole-cell recordings from PV and PYR neurons.

B, Representative whole-cell voltage-clamp recordings from L2/3 PYR neurons in S1 of mice with two ($PV^{Cre/WT}$; Ai14) and no ($Kcng4^{Cre/Cre}$; Ai14) active alleles of *Kcng4*. APs were evoked in tdTomato-positive, fast-spiking neurons by brief current injections (1–2 nA, 1 ms), resulting in inhibitory postsynaptic currents (IPSCs) in synaptically connected PYR neurons. A representative response to a single AP is displayed for each group.

C, IPSC peak amplitude measured as current (*i*; *left,* nA) or converted to conductance (*g*; *right,* nS) for wildtype (n=11/9 pairs/mice) and homozygous (n=10/8 pairs/mice) groups.

D, Representative response to two presynaptic action potentials (paired-pulse stimulation) delivered with an interstimulus interval of 10 ms, recorded as in **B**.

E, Paired-pulse ratio (PPR) of inhibitory current (*i*; *left*) and conductance (*g*; *right,* nS) across groups for ISIs of 10, 20, 50, 100, 200, 500, and 1000 ms.

F, Representative response to five presynaptic action potentials delivered with an interstimulus interval of 10 ms, recorded as in **B** and **D**.

G, Amplitude of inhibitory current (*i*; *left*) and conductance (*g*; *right*) across groups, normalized to response from the first AP, for an ISI (Δt) of 10 ms.

H, As in **G** for an ISI of 100 ms.

Mean ± SEM displayed. ** $P < 0.005$, * $P < 0.05$; NS: not statistically significant. Unpaired two-tailed t-tests or repeated-measures ANOVA (Greenhouse-Geisser corrected).

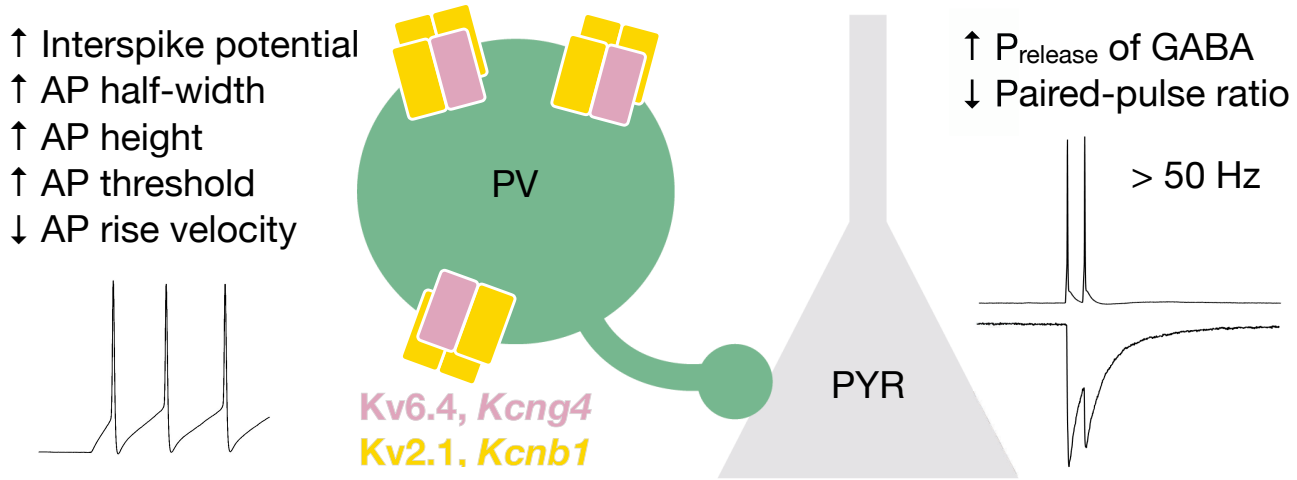
↑ Interspike potential
↑ AP half-width
↑ AP height
↑ AP threshold
↓ AP rise velocity
PV
Kv6.4, Kcng4
Kv2.1, Kcnb1
PYR
↑ P release of GABA
↓ Paired-pulse ratio
> 50 Hz

Figure 5. Model: Kv6.4 alters PV neuron waveform and inhibition of PYR neurons. Kv6.4 (*Kcng4*) forms a heterotetrameric potassium channel complex in PV neurons, which depolarizes interspike and threshold potentials, broadens AP duration, increases AP amplitude, and decelerates AP rise velocity. We propose that these waveform changes decrease the paired-pulse ratio of inhibition evoked in postsynaptic PYR neurons, reflecting the reduced paired-pulse depression observed, at short interstimulus intervals. Thus, Kv6.4 increases the probability of GABA release during high-frequency firing and thereby regulates the temporal precision of PV inhibitory output.

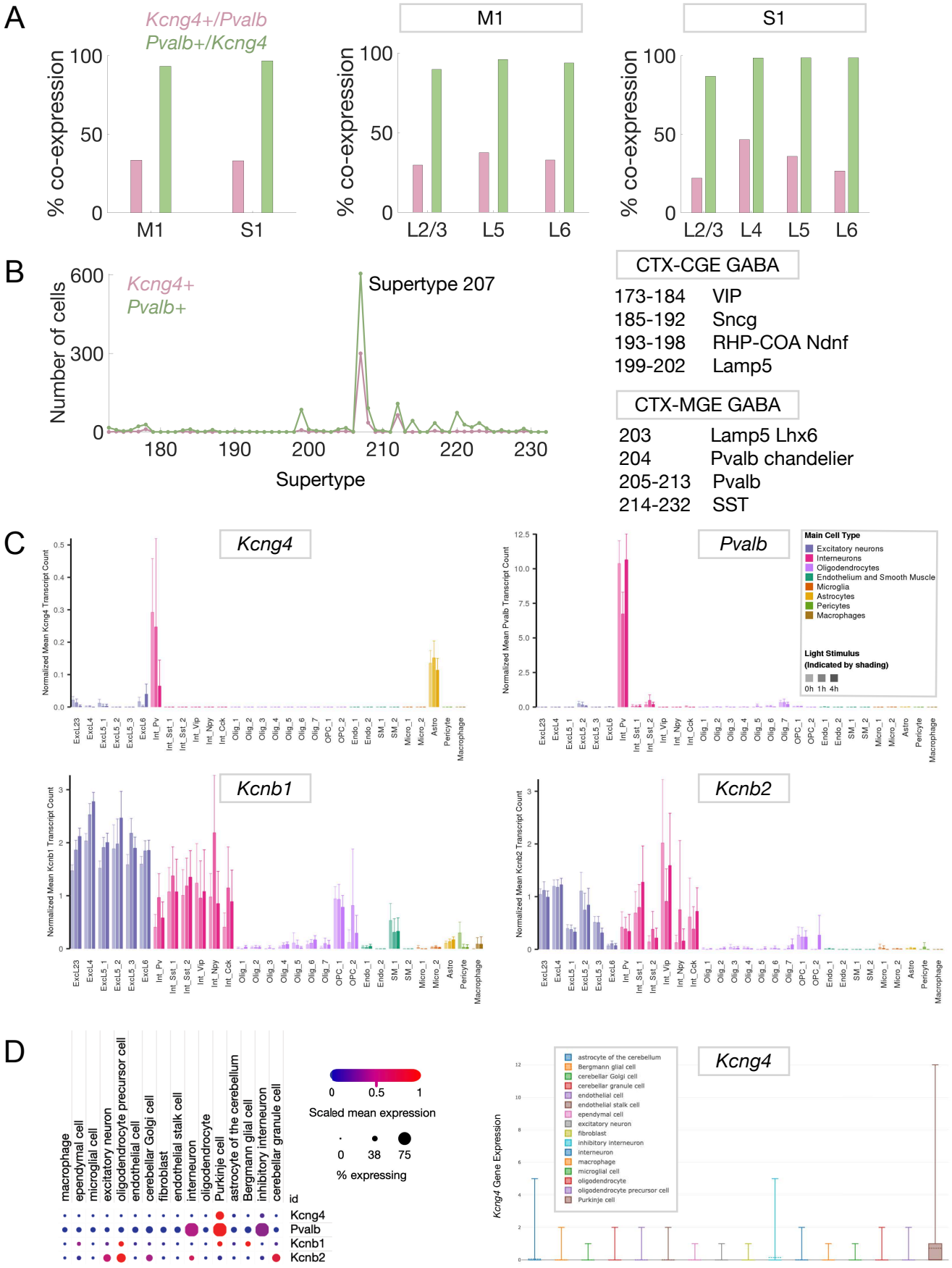
A
Kcng4+/Pvalb
Pvalb+/Kcng4
% co-expression
M1
S1
L2/3
L4
L5
L6
B
Kcng4+
Pvalb+
Number of cells
Supertype 207
Supertype
CTX-CGE GABA
173-184 VIP
185-192 Sncg
193-198 RHP-COA Ndnf
199-202 Lamp5
CTX-MGE GABA
203 Lamp5 Lhx6
204 Pvalb chandelier
205-213 Pvalb
214-232 SST
C
Kcng4
Pvalb
Kcnb1
Kcnb2
Normalized Mean Kcng4 Transcript Count
Normalized Mean Pvalb Transcript Count
Normalized Mean Kcnb1 Transcript Count
Normalized Mean Kcnb2 Transcript Count
Main Cell Type
Excitatory neurons
Interneurons
Oligodendrocytes
Endothelium and Smooth Muscle
Microglia
Astrocytes
Pericytes
Macrophages
Light Stimulus
(Indicated by shading)
0h 1h 4h
D
macrophage
ependymal cell
microglial cell
excitatory neuron
oligodendrocyte precursor cell
endothelial cell
cerebellar Golgi cell
fibroblast
endothelial stalk cell
interneuron
oligodendrocyte
Purkinje cell
astrocyte of the cerebellum
Bergmann glial cell
inhibitory interneuron
cerebellar granule cell
id
Kcng4
Pvalb
Kcnb1
Kcnb2
Scaled mean expression
% expressing
Kcng4 Gene Expression

Fig. S1. Co-expression and cell-type-specificity of *Kcng4* and *Pvalb* across spatial and single-cell transcriptomic datasets.

A, Quantification of cells co-expressing *Kcng4* and *Pvalb* in adult mouse cortex was performed using Multiplexed Error-Robust Fluorescence *In Situ* Hybridization (MERFISH) data from the Allen Brain Cell (ABC) Atlas (Zhuang-ABCA-1, MERFISH whole brain coronal 1), accessed via the Brain Knowledge Platform (10). Percentage of co-expressing cells in M1 and S1, labeling as in **Fig. 1E**.

B, Number of *Kcng4*- and *Pvalb*-expressing cells in S1 across PV neuron supertypes, as classified by the ABC Atlas (*left*). Legend detailing inhibitory subtypes (*right*). Abbreviations: CTX, cortex; CGE, caudal ganglionic eminence; MGE, medial ganglionic eminence; GABA, GABAergic neuron; VIP, vasoactive intestinal peptide; Sncg, synuclein, gamma; RHP, retrohippocampal region; COA, cortical amygdalar area; Ndnf, neuron-derived neurotrophic factor; Lamp5, lysosomal-associated membrane protein family, member 5; Lhx6, LIM homeobox protein 6; Pvalb, parvalbumin; SST, somatostatin.

C, Normalized transcript counts for *Kcng4*, *Pvalb*, *Kcnb1*, and *Kcnb2* across cell types in mouse adult visual cortex from single-cell RNA sequencing data (3) accessed via an interactive gene expression database.

D, Gene expression for *Kcng4*, *Pvalb*, *Kcnb1*, and *Kcnb2* across cell types in mouse adult cerebellar cortex from single-nuclei RNA sequencing data (6) with a detailed visualization of *Kcng4* gene expression, accessed via the interactive Single Cell Portal.

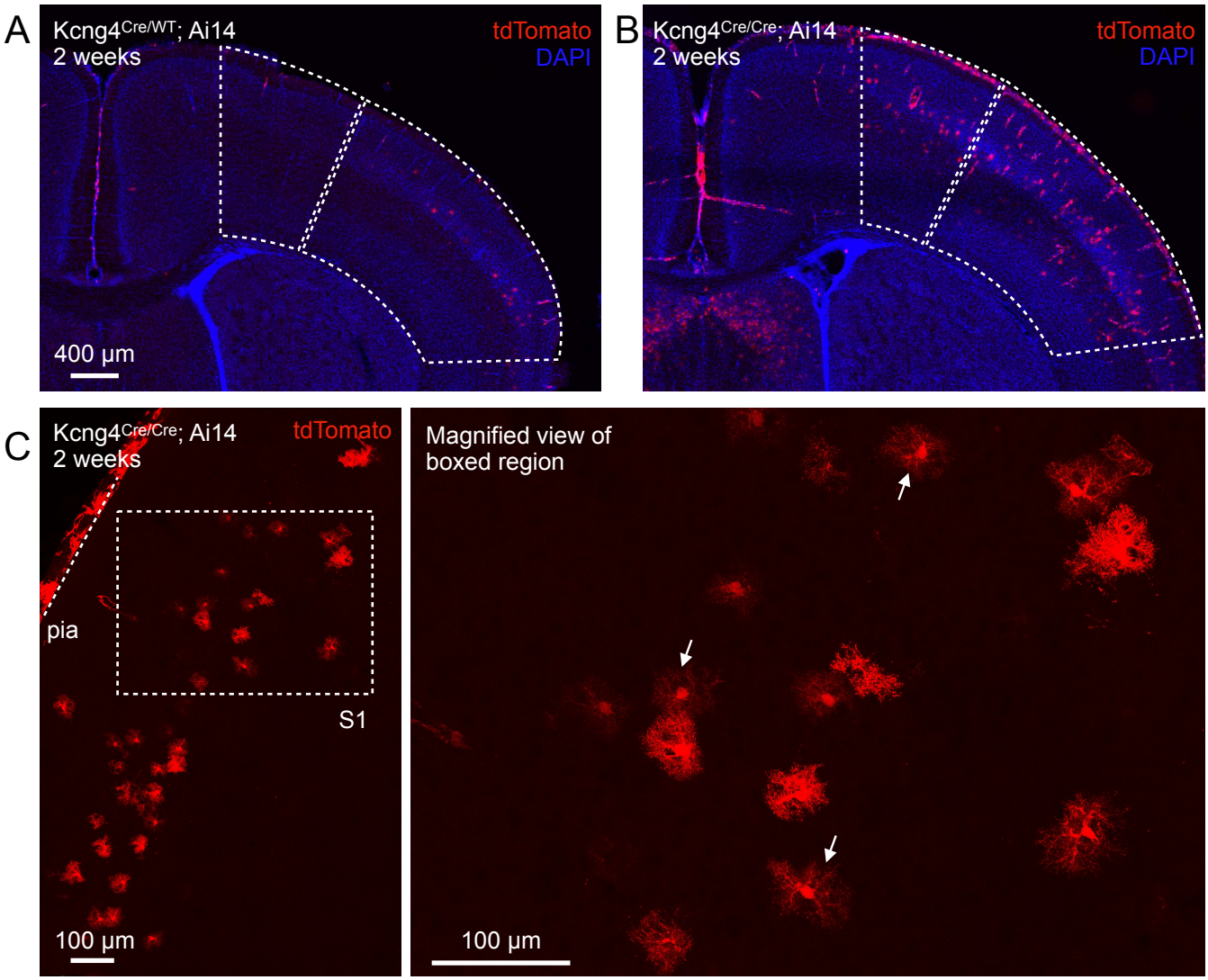
A
Kcng4Cre/WT; Ai14
2 weeks
tdTomato
DAPI
400 µm
B
Kcng4Cre/Cre; Ai14
2 weeks
tdTomato
DAPI
C
Kcng4Cre/Cre; Ai14
2 weeks
tdTomato
pia
S1
100 µm
Magnified view of
boxed region
100 µm

Fig. S2. Kcng4^{Cre} activation in juvenile mice.
A-B, Representative images showing tdTomato fluorescence in M1 and S1 for heterozygous (Kcng4$^{Cre/WT}$; Ai14) **(A)** and homozygous (Kcng4$^{Cre/Cre}$; Ai14) **(B)** mice at 2 weeks, corresponding to the regions outlined in **Fig. 2A**.
C, Higher magnification images illustrating the distribution of tdTomato-positive cells in S1 of a homozygous (Kcng4$^{Cre/Cre}$; Ai14) mouse. Magnified view (*right*) of the boxed region (*left*) marked by dashed white lines. Solid white arrows highlight example cells exhibiting astrocytic morphology (*right*).

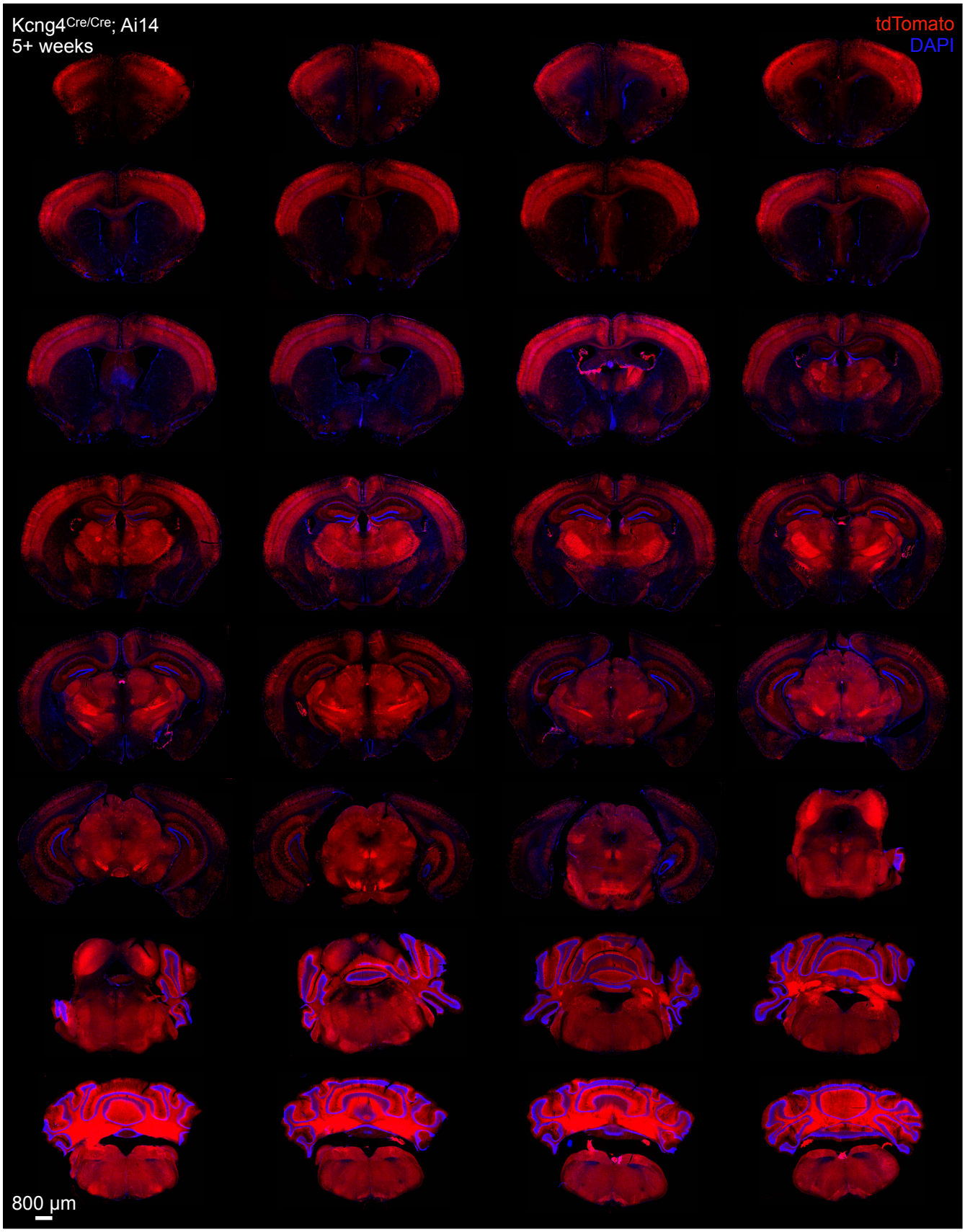
Kcng4Cre/Cre; Ai14
5+ weeks
tdTomato
DAPI
800 µm

Fig. S3. Brain-wide Kcng4^{Cre} activation in adult mice.
Representative images showing tdTomato fluorescence in a homozygous (Kcng4$^{Cre/Cre}$; Ai14) mouse at 5+ weeks across various brain areas, arranged anterior to posterior.

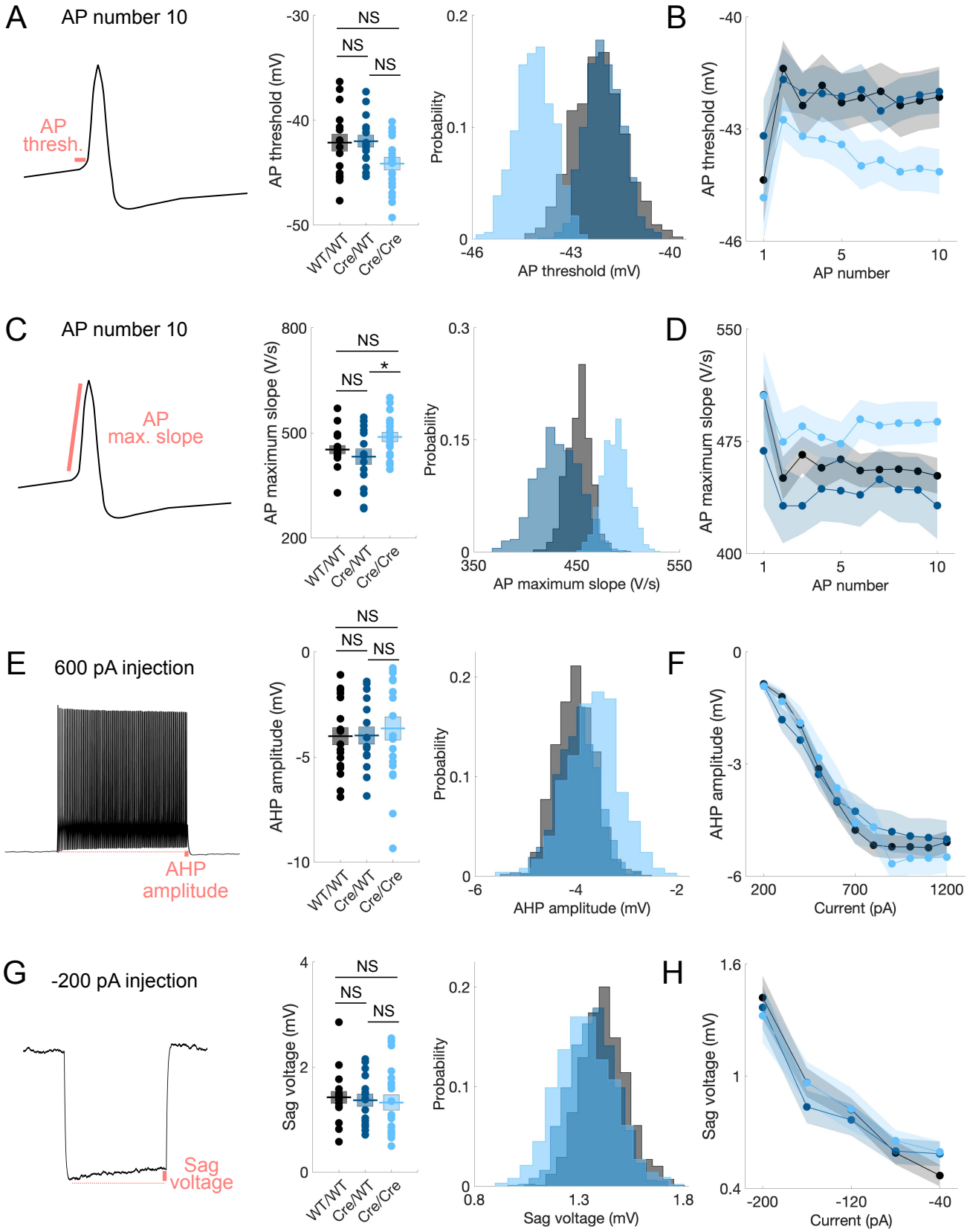
A
AP number 10
AP
thresh.
AP threshold (mV)
-30
-40
-50
NS
NS
NS
WT/WT
Cre/WT
Cre/Cre
Probability
0.2
0.1
0
-46
-43
-40
AP threshold (mV)
B
AP threshold (mV)
-40
-43
-46
1
5
10
AP number
C
AP number 10
AP
max. slope
AP maximum slope (V/s)
800
500
200
NS
NS
*
WT/WT
Cre/WT
Cre/Cre
Probability
0.3
0.15
0
350
450
550
AP maximum slope (V/s)
D
AP maximum slope (V/s)
550
475
400
1
5
10
AP number
E
600 pA injection
AHP
amplitude
AHP amplitude (mV)
0
-5
-10
NS
NS
NS
WT/WT
Cre/WT
Cre/Cre
Probability
0.2
0.1
0
-6
-4
-2
AHP amplitude (mV)
F
AHP amplitude (mV)
0
-3
-6
200
700
1200
Current (pA)
G
-200 pA injection
Sag
voltage
Sag voltage (mV)
4
2
0
NS
NS
NS
WT/WT
Cre/WT
Cre/Cre
Probability
0.2
0.1
0
0.8
1.3
1.8
Sag voltage (mV)
H
Sag voltage (mV)
1.6
1
0.4
-200
-120
-40
Current (pA)

Fig. S4. Additional intrinsic properties of PV neurons following Kv6.4 deletion.
A, Schematic of AP threshold (*left*), group means (mV, *center*), and bootstrapped distribution of the means (*right*) for the 10th AP, as described in **Fig. 3**.
B, Mean values across the first 10 APs (mV).
C-H, As in **A** and **B** for AP maximum slope (V/s) (**C-D**), afterhyperpolarization (AHP; mV) amplitude (**E-F**), and sag voltage (mV) (**G-H**).
AHP amplitude was measured from a current injection of 600 pA (**E**) and across stepwise current injections from 200 to 1200 pA (**F**). AHP amplitude was defined as the difference between the resting membrane potential and the most negative voltage following current injection. Sag voltage was measured from a current injection of -200 pA (**G**) and across hyperpolarizing steps from -200 to -40 pA (**H**). Sag voltage was defined as the difference between the steady-state voltage and peak hyperpolarization during hyperpolarizing current injections.
Mean ± SEM displayed. * $P < 0.05$; NS: not statistically significant. One-way ANOVA (Tukey-Kramer post hoc multiple comparisons). Bootstrapping (1,000 iterations) was used to visualize sample mean distributions.

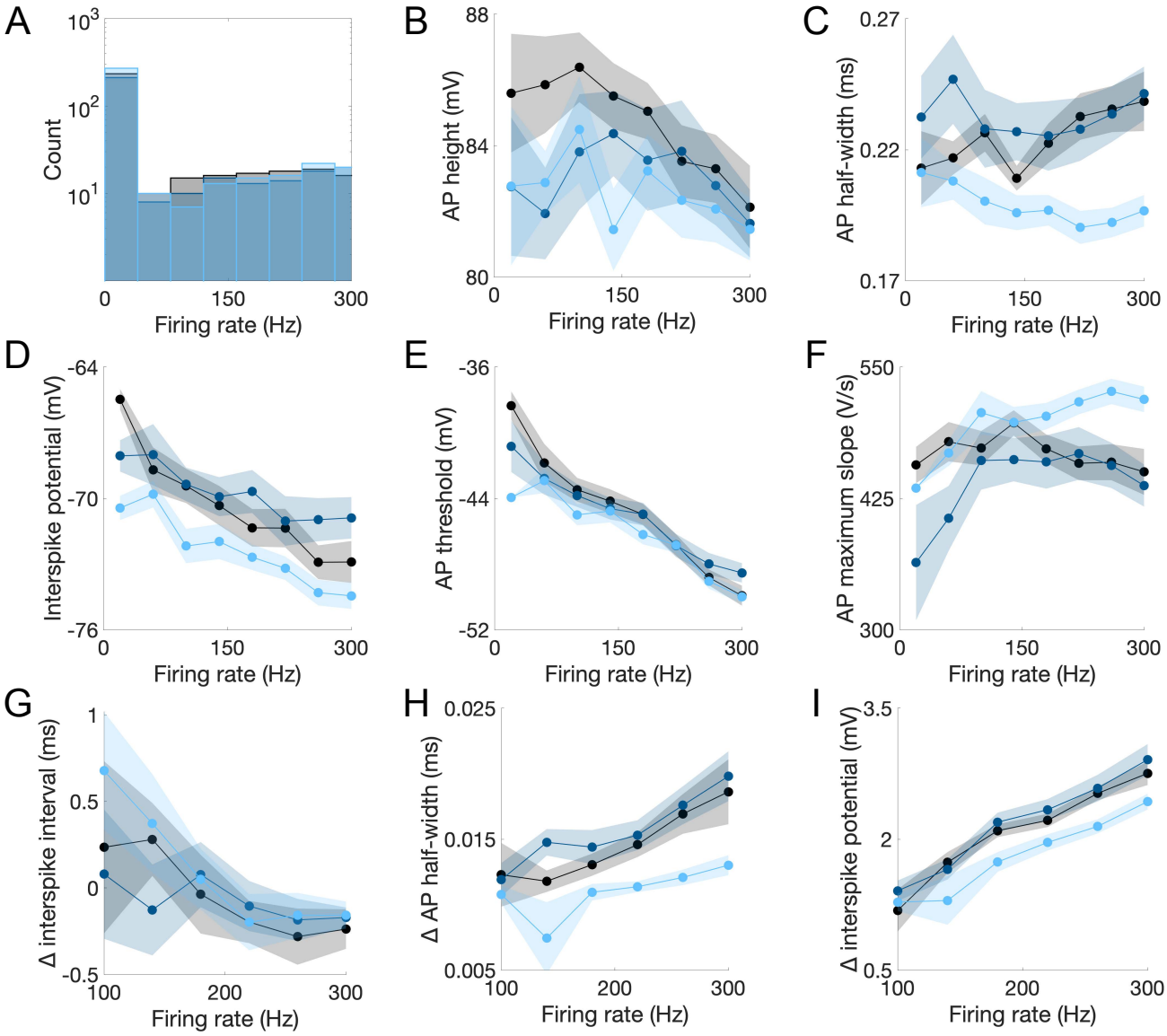
A
Count
Firing rate (Hz)
B
AP height (mV)
Firing rate (Hz)
C
AP half-width (ms)
Firing rate (Hz)
D
Interspike potential (mV)
Firing rate (Hz)
E
AP threshold (mV)
Firing rate (Hz)
F
AP maximum slope (V/s)
Firing rate (Hz)
G
Δ interspike interval (ms)
Firing rate (Hz)
H
Δ AP half-width (ms)
Firing rate (Hz)
I
Δ interspike potential (mV)
Firing rate (Hz)

Fig. S5. Extended analysis of PV intrinsic properties following Kv6.4 deletion.
A, Histogram of firing rate (Hz) distribution (within 300 Hz) for all recordings, independent of current injection, across groups described in **Fig. 3**.
B, AP height (mV) across firing rate for all recordings.
C-F, As in **B** for AP half-width (ms) (**C**), interspike potential (mV) (**D**), AP threshold (mV) (**E**), and AP maximum slope (V/s) (**F**).
G, Change (Δ) in interspike interval (ISI; ms), defined as $ISI_{49-50} – ISI_{2-3}$, across firing rate in recordings containing ≥50 APs.
H-I, As in **G**, for Δ AP half-width (ms), defined as AP_{50} half-width – AP_2 half-width (**H**), and Δ interspike potential (mV), defined as AP_{50} interspike potential – AP_2 interspike potential (**I**).
Mean ± SEM displayed.

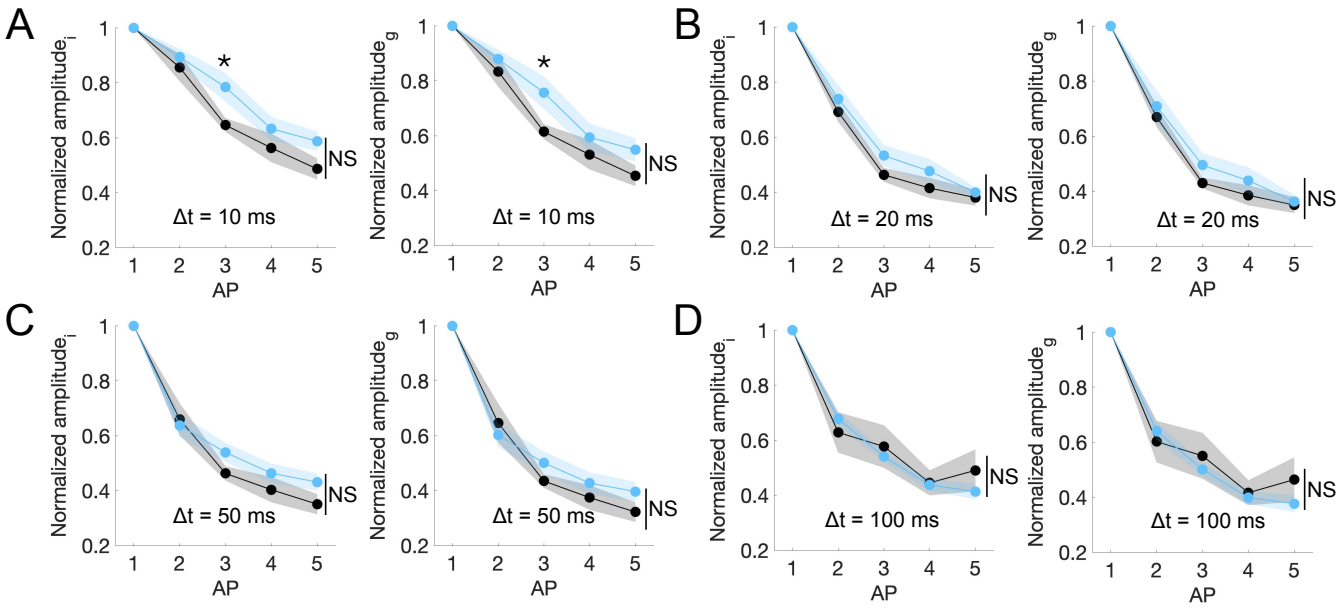
A
B
C
D
Normalized amplitude$_i$
Normalized amplitude$_g$
AP
Δt = 10 ms
Δt = 20 ms
Δt = 50 ms
Δt = 100 ms
NS
*

Fig. S6. Paired pulse depression at PV-PYR synapses across varying interstimulus intervals following Kv6.4 deletion.

A-D, Amplitude of inhibitory current (i; *left*, pA) and conductance (g; *right*, nS) across groups, normalized to response from the first AP, during trains of five presynaptic action potentials, as described in **Fig. 4**. Trains were delivered with an ISI (Δt) of 10 ms (**A**), 20 ms (**B**), 50 ms (**C**), and 100 ms (**D**).

Mean ± SEM displayed. * $P < 0.05$; NS: not statistically significant. Unpaired two-tailed t-tests or repeated-measures ANOVA (Greenhouse-Geisser corrected).

Datasets

Dataset S1 (separate file). Raw data and summary data for Fig. 1 and Fig. S1.

Dataset S2 (separate file). Summary data for Fig. 3 and Fig. S4.

Dataset S3 (separate file). Summary data for Fig. 4 and Fig. S6.